

# **Optimization of Superaustenitic Stainless Steel Filler Metals for Welding Advanced Double Hull Combatant Ships**

Feb. 16, 2005

Report Prepared by  
T.D. Anderson, K.D. Adams, M.J. Perricone, J.N. DuPont, and A.R. Marder  
Lehigh University  
Engineering Metallurgy Group  
5 E. Packer Ave.  
Bethlehem, PA 18015

for

Office of Naval Research  
One Liberty Center  
875 North Randolph Street, Suite 1425  
Arlington, VA 22203-1995  
under contract N00014-03-1-0348

**DISTRIBUTION STATEMENT A**  
Approved for Public Release  
Distribution Unlimited

## REPORT DOCUMENTATION PAGE

Form Approved  
OMB No. 0704-0188

The public reporting burden for this collection of information is estimated to average 1 hour per response, including the time for reviewing instructions, searching existing data sources, gathering and maintaining the data needed, and completing and reviewing the collection of information. Send comments regarding this burden estimate or any other aspect of this collection of information, including suggestions for reducing the burden, to Department of Defense, Washington Headquarters Services, Directorate for Information Operations and Reports (0704-0188), 1215 Jefferson Davis Highway, Suite 1204, Arlington, VA 22202-4302. Respondents should be aware that notwithstanding any other provision of law, no person shall be subject to any penalty for failing to comply with a collection of information if it does not display a currently valid OMB control number.

**PLEASE DO NOT RETURN YOUR FORM TO THE ABOVE ADDRESS.**

1. REPORT DATE (DD-MM-YYYY) 16-Feb-06			2. REPORT TYPE Final		3. DATES COVERED (From - To) 01-Jan-03 to 31-Dec-05	
4. TITLE AND SUBTITLE  Optimization of Superaustenitic Stainless Steel Filler Metals for Welding Advanced Double Hull Combatant Ships			5a. CONTRACT NUMBER  5b. GRANT NUMBER N00014-03-1-0348 5c. PROGRAM ELEMENT NUMBER  5d. PROJECT NUMBER  5e. TASK NUMBER  5f. WORK UNIT NUMBER			
6. AUTHOR(S) Timothy Anderson Kenneth Adams Dr. Matthew Perricone Dr. John DuPont Dr. Arnold Marder						
7. PERFORMING ORGANIZATION NAME(S) AND ADDRESS(ES)  Lehigh University Materials Science and Engineering Department 5 E. Packer Ave. Bethlehem, PA 18015			8. PERFORMING ORGANIZATION REPORT NUMBER			
9. SPONSORING/MONITORING AGENCY NAME(S) AND ADDRESS(ES)  Office of Naval Research 800 N. Quincy St. Arlington, VA 22217			10. SPONSOR/MONITOR'S ACRONYM(S) ONR 11. SPONSOR/MONITOR'S REPORT NUMBER(S)			
12. DISTRIBUTION/AVAILABILITY STATEMENT Approved for public release; distribution is unlimited.						
13. SUPPLEMENTARY NOTES						
14. ABSTRACT  The performance of welds on superaustenitic stainless steels (SASS) such as AL-6XN has been improved through the use of a new microstructural development sequence. Thermodynamic calculations were used to isolate the range of possible filler metal compositions, the results of which were confirmed experimentally through alloy construction and EPMA analysis. HED welds on the alloys were used to induce the massive transformation, which is capable of producing fully-austenitic welds with uniform distributions of Mo. SASS welds using such a filler metal should display improved corrosion resistance and weldability over current Ni-base filler metal solutions. The tensile, fracture toughness, and fatigue properties of AL-6XN plate material in the short-transverse (S-T) orientation were studied. The presence of brittle second-phase particles in the form of microstructural packets has been shown to be detrimental to the mechanical properties of AL-6XN.						
15. SUBJECT TERMS superaustenitic stainless steels; CALPHAD; massive transformations; solidification behavior; solid-state transformations;						
16. SECURITY CLASSIFICATION OF: a. REPORT		b. ABSTRACT	c. THIS PAGE	17. LIMITATION OF ABSTRACT UU	18. NUMBER OF PAGES 57	19a. NAME OF RESPONSIBLE PERSON Dr. John DuPont 19b. TELEPHONE NUMBER (Include area code) 610-758-3942

<b>ABSTRACT</b>	iii
<b>1. Filler Metal Research</b>	1
1.1 Background	1
1.2 Experimental Procedure	4
1.3 Results	8
<i>1.3.1 Phase Stability Diagrams</i>	8
<i>1.3.2 Model Validation and Microstructural Characterization</i>	9
<i>1.3.3 Sigma Phase</i>	12
<i>1.3.4 Solute Distribution</i>	13
<i>1.3.5 Higher-Order Alloys</i>	15
<i>1.3.6 HED Welds</i>	18
<b>2. Mechanical Behavior Research</b>	21
2.1 Background	21
2.2 Experimental Procedure	22
2.2 Results and Discussion	26
<i>2.2.1 Tensile Testing</i>	26
<i>2.2.2 Fracture Toughness Testing</i>	31
<i>2.2.3 Apparent Fracture Process</i>	37
<i>2.2.4 Fatigue Testing</i>	37
<b>Reference List</b>	41

## ABSTRACT

The excellent corrosion resistance of superaustenitic stainless steel (SASS) alloys has been shown to be a direct consequence of high concentrations of molybdenum (Mo). It has been shown that the microsegregation of Mo that occurs during austenitic solidification can lead to preferential corrosive attack at dendrite cores. Research was conducted to locate possible Fe-based compositions for a filler metal that will circumvent these issues. The distribution of Mo has been improved through the use of a ferritic solidification mode, the structure of which can become austenitic via a solid-state phase transformation that occurs during post-solidification cooling of the weld. This work successfully located the range of alloy compositions that will experience this type of microstructural development through the use of thermodynamic calculation software. Confirmation of the phase transformation sequence was achieved through construction of a matrix of experimental alloys using the arc-button melting technique. Microstructural characterization and EPMA analysis of the alloys corroborated the predictions of CALPHAD-based diagrams and verified the improved concentrations of Mo in austenite. The effect of a higher cooling rate in welds of these alloys was also observed in HED welds deposited directly on the alloy buttons. Another mode of the solid-state ferrite-to-austenite transformation, the so-called massive transformation, was observed to produce fully-austenitic structures from alloys that solidified primarily as ferrite. The lack of solute partitioning characteristic of the massive transformation was shown in EPMA traces displaying uniform distributions of Mo at concentrations matching the nominal.

Current data on the experimental alloys predicts improved corrosion resistance and weldability of welds conducted on SASS alloys relative to properties shown by Ni-based filler metal welds. Successful completion of corrosion testing and solidification cracking studies could yield a promising filler metal that could produce welds with significantly improved performance, while simultaneously being a source of appreciable cost savings. Moreover, studies on the massive transformation in these welds could potentially widen the applications for such a filler metal. The fully-austenitic structures attainable through this mechanism show Mo distributions previously beyond reach.

In addition to filler metal development for welding the superaustenitic stainless steel AL-6XN, the tensile, fracture toughness, and fatigue properties of AL-6XN plate material in the short-transverse (S-T) orientation were studied. The material was specifically tested with respect

to the presence or absence of microstructural ‘packets’ of brittle  $\sigma$ -phase particles within the matrix, at and surrounding the centerline of the plate. Tensile specimens containing these packets of  $\sigma$ -phase particles exhibited reduced yield and tensile strengths as well as pronounced reduction in ductility compared to specimens free of the packets. The fracture toughness (J-R resistance-curve) data indicate that the presence of the packets is a detriment to the fracture toughness of the material in the S-T orientation. The fracture toughness response in the longitudinal-transverse (L-T) and transverse-longitudinal (T-L) orientations from a separate plate, also containing similar microstructural packets near the centerline of the plate, was found to be tougher than both S-T sample conditions. Fatigue tests displayed similar behavior for all samples containing the microstructural packets and a slight improvement was observed for samples free of the packets. The cause for the improved behavior in the packet-free samples is most likely a result of the larger average grain size encountered in the region of the sample that the fatigue crack traversed. The fatigue cracks in the packet-containing S-T samples were not observed to encounter many packets, none of which were encountered in any cross-sections of the samples where the crack position correlates to the threshold region of fatigue crack growth. Overall, the presence of brittle second-phase particles in the form of microstructural packets has been shown to be detrimental to the mechanical properties of AL-6XN, however, the fatigue behavior in the presence of the packets is indiscernible.

## **1. Filler Metal Research**

### ***1.1 Background***

The Office of Naval Research (ONR) is currently investigating the use of Super-Austenitic Stainless Steels (SASS) for Advanced Double Hull (ADH) combatant ships. As shown in Figure 1, this approach involves a change in both alloy and hull design compared to the current single hull ships constructed from low alloy steel. The use of a SASS alloy combined with the ADH design can provide significant advantages. For example, the ADH design provides an appreciable reduction in fabrication cost because of the simplified design. These savings have been estimated at \$60 million for a DDG-51 ship<sup>1</sup>. The double hull design also increases survivability by providing a second, inner hull. The superior corrosion resistance of the SASS alloy can reduce or eliminate periodic inspection and maintenance associated with hull corrosion, thus decreasing the life-cycle maintenance cost. The superior toughness of the SASS also provides an additional improvement in survivability. Lastly, and perhaps most importantly, the fully austenitic structure of the SASS alloy eliminates magnetic signatures, thus making combatant ships undetectable by mines.

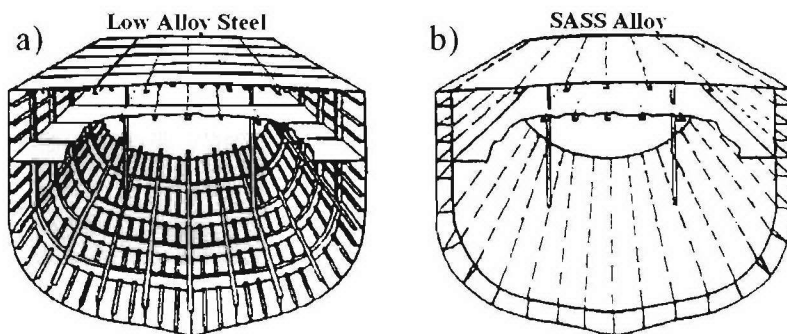


**Figure 1. Illustration of a) single hull and b) advanced double hull designs.**

Fusion welding is a major fabrication step during construction of SASS-ADH ships. The influence of welding on the performance of SASS requires careful consideration to ensure the potential advantages of this relatively new alloy are realized for ADH applications. The current approach to arc welding of SASS alloys involves the use of overalloyed nickel base alloys that are high in molybdenum (Mo). The relatively high Mo concentration helps compensate for Mo

microsegregation in the weld that is responsible for localized, accelerated corrosion attack. Work performed previously at Lehigh University<sup>2-4</sup> has shown that the weld metal composition, segregation behavior, corrosion resistance, and weldability will strongly depend on the welding parameters used to deposit the nickel base filler metal. Thus, with this approach, careful control over processing parameters is vital to depositing defect-free welds with acceptable corrosion resistance. While the use of overalloyed nickel base filler metals provides a short-term approach, there are several major drawbacks, such as 1) Microsegregation can not be avoided in nickel base alloys, 2) The fully austenitic alloys are susceptible to solidification cracking, 3) Precise control over welding parameters is required for composition control, which can be difficult in a shipyard environment where a wide range of plate thicknesses and joint designs are encountered, 4) Nickel base alloys are significantly more expensive than stainless steels, and 5) a galvanic couple is produced between the nickel base weld and iron base parent metal that may accelerate corrosion.

The work performed at Lehigh University under the current project has demonstrated the potential for developing a new filler metal that would eliminate the drawbacks described above. The technique by which this was accomplished was by way of a two-stage process:

### *1) Primary solidification of the ferrite phase*

The primary solidification of ferrite can solve many of the problems associated with the solidification of SASS welds that employ Ni-based filler metals and solidify as austenite. The loss of corrosion resistance in the Ni-based welds is the result of microsegregation, a process that pushes the critical alloying element Mo into the liquid during solidification. The result is a cored solidification structure, in which the cell cores that are the first to solidify are depleted in Mo and are thus susceptible to preferential corrosion<sup>5</sup>. The Mo solute is unable to diffuse down the concentration gradient, because austenite possesses a close-packed fcc structure which severely limits the rates of atomic diffusion. The crystal structure of ferrite, however, is not as close-packed, and can allow the backdiffusion of Mo. This enhanced diffusion of Mo in ferrite eliminates the Mo concentration gradients, leaving a structure with a uniform distribution of elements that contains no preferential sites for corrosive attack.

The bcc structure of ferrite is also effective at reducing the incidence of solidification cracking. The elements phosphorus (P) and sulfur (S) do not readily dissolve in the close-packed

structure of austenite, and thus will accumulate in the final liquid to solidify. High concentrations of P and S are well known to drive the melting temperature in this region to much lower temperatures. The film of liquid that remains cannot sustain the shrinkage strains that arise during fusion welding, and will often lead to the creation of a solidification crack<sup>6</sup>. Once again, the more open structure of bcc-ferrite can dissolve the adverse elements P and S, preventing them from creating a low-melting point phase that is responsible for cracking. The elevated ductility and lower thermal expansion coefficient of ferrite also assist in reducing the overall mechanical stresses that develop during weld solidification<sup>6</sup>.

## 2) *Solid-state transformation to the austenite phase*

While the primary solidification of ferrite can lead to advantages over austenitic solidification, such a weld zone would exhibit a magnetic signature and mechanical properties dissimilar to that of the surrounding base metal. The ideal weld zone will have properties that match the base metal, so as to provide continuity between the joined members. The joining of SASS alloys demands a weld zone microstructure composed predominately of austenite. Fortunately, the phase diagram of the Fe-Ni-Cr-Mo quaternary system provides the opportunity for alloys that solidify as primary ferrite to undergo a solid-state transformation to the austenite phase during cooling. The vertical section in Figure 2a shows the sloping solvus that is present below the eutectic line of the Fe-Ni-Cr-Mo phase diagram. Alloys to the right of the eutectic line (A) solidify as ferrite, but later cool into the single-phase region of the phase diagram where only austenite is stable. This instability of ferrite will cause it to transform into austenite by one of several solid state mechanisms<sup>6,7</sup>.

Development of a filler metal that exhibits this two-stage transformation sequence will be very beneficial in several ways. The improvement of corrosion resistance and reduction of solidification cracking will lead to longer lifetimes for the welded structure, and reduce the overall monetary costs and vessel downtime associated with hull maintenance. The weld zones will also be Fe-based, which can curtail the possibility of galvanic couples that would form between a Ni-based weld and a Fe-based base metal which may lead to accelerated corrosion. The Fe-based composition of such a filler metal is further advantageous based on the possible material cost savings. A filler metal composed principally of Ni will always be more expensive than one based on ferrous stainless steel compositions.

The work completed recently at Lehigh University sought to identify compositions that will develop in the manner described above. Improved methods of modeling the alloy system, using thermodynamic computational software, were first used to identify candidate compositions. A wide matrix of experimental alloys was then constructed both to validate the modeling results and to attain samples for detailed microstructural characterization. The wide range of compositions studied allowed several conclusions to be made concerning the compositional window within which the desired development sequence occurs. Examination of solute distribution confirmed the advantageous qualities of the solid-state transformation to austenite relative to the distributions that result from the solidification of austenite. In addition, further research was performed on the experimental alloys to observe the effects of cooling rate in the weld on the phase transformation sequence and concomitant microstructure. Another mechanism of transformation was discovered to occur at high cooling rates which may further improve upon the two-step microstructural development sequence. This massive transformation has been shown produce *fully-austenitic* structures with complete uniformity in elemental distribution. The lack of partitioning in this transformation mechanism renders the entire product phase essentially continuous in Mo concentration; hence corrosion resistance will be maximized. Results from this research are summarized in more detail below.

## ***1.2 Experimental Procedure***

A large matrix of vertical isopleths was constructed of the Fe-Ni-Cr-Mo system using the CALPHAD software Thermo-Calc<sup>8</sup> in conjunction with the Iron Alloy Database<sup>9</sup>. The bcc (ferrite) and fcc (austenite) phases were included in the initial calculations, and a range of temperatures was used that would span from the fully liquid state to any solid-state phase transformations that might transpire. The software package allows specific portions of a generated diagram to be enlarged; this feature was used to acquire the specific temperature and composition of four special points of interest:

- a. Eutectic composition
- b. Ferritic vertex of the eutectic triangle
- c. Austenitic vertex of the eutectic triangle
- d. Maximum solid solubility of Cr in austenite

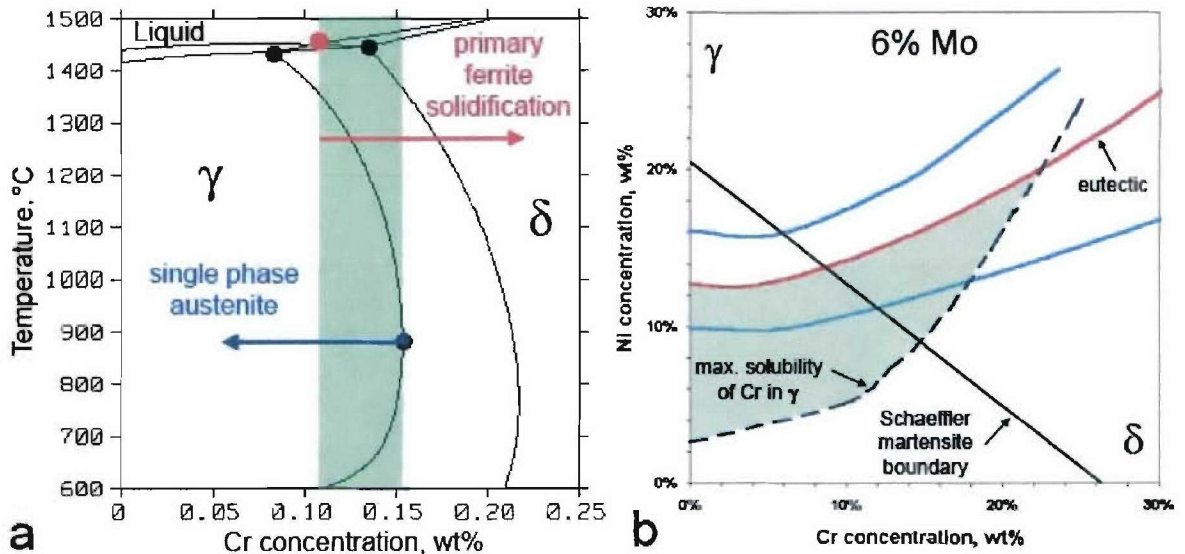


**Figure 2.** Two separate views of the Fe-Ni-Cr-Mo phase diagram: a) vertical isopleth displaying the post-solidification behavior for a set of constant-Fe, constant-Mo alloys; b) the phase stability diagram for all compositions with 6wt% Mo. The green shaded zones in each figure represent the range of predicted FA solidification mode.

Figure 2a illustrates the locations of these points of interest on a sample isopleth. By plotting these points on the axes of a liquidus projection, a top-down view of the phase diagram was created (Figure 2b) that permitted observation of both the solidification behavior and the likelihood of subsequent solid-state transformation over a much broader composition range than was previously possible. The temperature axis is normal to the plane of the diagram. The martensite boundary from the Schaeffler Diagram<sup>10</sup> was also incorporated onto the diagrams. The use of these diagrams will be discussed in more detail in the next section.

Experimental study of the alloy system and verification of the new diagrams was sought through laboratory experiment. Sixteen compositions spanning both sides of the eutectic line in each of the six modeled Mo contents, for a total of 96 experimental alloys, were selected for construction. The target compositions of these alloys are given in Table I. The alloys were produced from virgin elements using a Thermal Technologies BJ-5 Arc-Button Melter. Carefully weighed portions of each constituent were placed in a chamber under vacuum, which was then backfilled with inert argon to serve as a shielding gas. A manually-controlled TIG torch running at 300A and 10V were used to produce 50g buttons upon a water-cooled copper hearth. Wet-chemical testing using inductively-coupled plasma (ICP) analysis was later performed on each melt button. The results showed a typical variation of less than 0.5wt% for

each alloying element. The effectiveness of cooling system that prevented alloy contamination from the melting hearth was proven in the low (~0.01wt%) Cu concentrations that were detected. Combustion analyses were also performed on a subset of the alloys that demonstrated the efficacy of the inert atmosphere in preventing unintentional contamination from gaseous elements. Thus, the arc-button melting system was confirmed as a consistent source of high-purity experimental alloys.

Experiments involving elevated cooling rates were also conducted using the experimental alloy buttons. The bottom surface of each button was polished flat with 60-grit SiC paper to provide a surface smooth enough to deposit high-energy density welds. An OPTOMECH Nd-YAG Laser Deposition System was used to run three welds on each button at travel speeds of 10, 50, and 100 ipm – corresponding to speeds of 4.2, 21, and 42 mm/s. The laser power was set to 500W, while the power at the button surface was measured at 370W by a “power puck” calorimeter. The different travel speeds were deemed sufficient to attain a wide range of solidification velocities and thus cooling rates. Weld passes were conducted at a constant width apart (5 mm) in order to prevent overlap of elevated temperature fields.

Metallographic preparation and subsequent microstructural analysis were used to reveal and identify the particular solidification and transformation mechanisms experienced by each alloy. Alloys were polished using only SiC papers and  $\text{SiO}_2$  solution. Electrolytic etching was performed to reveal both button and weld microstructures using a mixture of 60%  $\text{HNO}_3$  and 40% water at voltages ranging from 2-3V in three second intervals. The relative locations and shape of the ferrite and austenite phases were used as indications of the solidification mode and morphological type in a manner previously described by Elmer<sup>7</sup>. The cooling rate in all four solidification conditions (arc-melt button, 3 laser welds) was estimated from measurement of the primary dendrite arm spacing. A technique developed by Katayama and Matsunawa<sup>11</sup> and later demonstrated by several authors<sup>7</sup> correlates the cooling rate  $\epsilon$  of a weld structure to the primary arm spacing  $\lambda$  in 310 stainless steel by the relationship:

$$\lambda = 80\epsilon^{-\frac{1}{3}}$$

in which  $\lambda$  is given in  $\mu\text{m}$  and  $\epsilon$  is given in  $^{\circ}\text{C/s}$ . The approach was considered appropriate given the similar compositions of the experimental alloys and 310 stainless steel.

**Table I.** Compositions of alloys generated in this study via arc-button melting. The solidification mode and ferrite content of each alloy is also given. The solidification mode of martensitic samples has been omitted and replaced with ‘M’.

Mo	Ni+Cr	Cr	Ni	Fe	Structure	%Ferrite	Mo	Ni+Cr	Cr	Ni	Fe	Structure	%Ferrite
0	20	10	10	80	M	58.1	6	20	4	16	74	M	44.3
		12	8	80	M	55.7			8	12	74	M	42.4
		14	6	80	M	56.4			10	10	74	M	48.7
		16	4	80	M	56.0			14	6	74	M	76.2
	25	13	12	75	M	40.9		25	9	16	69	A	0.0
		15	10	75	M	47.3			11	14	69	AF	0.2
		17	8	75	M	49.2			13	12	69	FA	5.3
		19	6	75	M	75.9			15	10	69	F	13.0
	30	16	14	70	A	0.0		30	12	18	64	A	0.0
		18	12	70	FA	2.3			14	16	64	AF	0.1
		20	10	70	F	10.5			16	14	64	FA	6.5
		22	8	70	F	55.1			18	12	64	F	14.4
	35	18	17	65	A	0.0		35	16	19	59	A	0.0
		20	15	65	AF	0.2			18	17	59	AF	0.5
		22	13	65	FA	9.2			20	15	59	F	12.2
		24	11	65	F	19.2			22	13	59	F	38.9
2	20	8	12	78	M	57.6	8	20	2	18	72	M	35.6
		10	10	78	M	57.4			6	14	72	M	31.6
		12	8	78	M	54.1			8	12	72	M	33.0
		16	4	78	M	82.2			12	8	72	M	63.7
	25	11	14	73	M	0.1		25	7	18	67	A	0.0
		13	12	73	M	20.1			9	16	67	A	0.0
		15	10	73	M	34.5			13	12	67	F	3.0
		17	8	73	M	44.7			15	10	67	F	26.9
	30	14	16	68	A	0.0		30	11	19	62	A	0.0
		16	14	68	AF	0.6			13	17	62	A	0.0
		18	12	68	FA	7.9			15	15	62	FA	1.9
		20	10	68	F	15.3			17	13	62	F	14.5
	35	18	17	63	AF	0.2		35	14	21	57	A	0.0
		20	15	63	FA	5.4			17	18	57	A	0.0
		22	13	63	F	14.2			20	15	57	F	13.2
		24	11	63	F	50.3			22	13	57	F	48.2
4	20	6	14	76	M	53.5	10	20	2	18	70	M	12.3
		8	12	76	M	51.4			4	16	70	M	21.5
		12	8	76	M	52.4			8	12	70	M	8.0
		14	6	76	M	75.3			12	8	70	M	65.8
	25	9	16	71	A	0.0		25	5	20	65	A	0.0
		11	14	71	A	0.0			9	16	65	A	0.0
		13	12	71	AF	1.4			13	12	65	F	4.8
		17	8	71	F	50.5			15	10	65	F	40.6
	30	13	17	66	A	0.0		30	10	20	60	A	0.0
		15	15	66	AF	0.4			12	18	60	A	0.0
		17	13	66	FA	7.3			14	16	60	FA	0.4
		19	11	66	F	17.8			16	14	60	F	9.0
	35	16	19	61	A	0.0		35	14	21	55	A	0.0
		18	17	61	AF	0.7			16	19	55	A	0.0
		20	15	61	FA	9.8			18	17	55	FA	0.0
		22	13	61	F	17.4			20	15	55	F	8.4

A magnetic ferrite detector was used to determine the specific weight percentage of ferrite within each alloy button. The small dimensions of the HED weld zones prevented direct measurement of their ferrite content. Precision was maintained through the use of calibrated standards of known ferrite content. These data, given with the corresponding compositions in Table I, were used to relate composition to the ferrite content. The related data of solidification mode and measured ferrite content were also plotted on the respective phase stability diagram for ease of comparison.

Electron microscopy was also utilized for analysis of solute distribution and phase identification. Electron Probe Micro-Analysis (EPMA) analysis was conducted using a JEOL 733 Superprobe equipped with four WDS spectrometers. Tests were performed on selected buttons and weld structures to observe the elemental distribution produced by each manner of microstructural development. Appropriate correction schemes were used to convert raw data to weight percentages for each element. Phase identification was performed using the electron-backscattered diffraction (EBSD) system equipped on an FEI Dual Beam 235 Focused Ion Beam milling station. Comparing the acquired pattern with crystallographic databases allowed for distinction of fcc ( $\delta$ -ferrite), bcc ( $\gamma$ -austenite), and tetragonal ( $\sigma$ -phase) crystal structures.

## 1.3 Results

### 1.3.1 Phase Stability Diagrams

An example of a multi-component phase stability diagram is shown in Figure 2b. The red line represents the eutectic line that separates the  $\gamma$ -austenite and  $\delta$ -ferrite primary solidification modes. The blue lines represent the edges of the Liquid +  $\delta$  +  $\gamma$  eutectic triangle. The dashed line that eventually intersects the eutectic line represents the maximum solubility of Cr in austenite. Successively higher additions of Mo cause the eutectic triangle not only to widen, but also to veer its location towards higher Ni contents, as shown in Figure 3. The latter effect is a result of the ferrite-stabilizing effect of Mo, comparable to that of Cr. In addition, the continued addition of Mo widens the space between the eutectic and the boundary representing the maximum solubility of Cr in austenite. Within this range, an alloy that solidifies as primary ferrite can cool into a region of the phase diagram in which only single-phase austenite is stable, thus exhibiting the thermodynamic potential for a ferrite to austenite solid state transformation.

The phase stability diagrams can be used to predict the solidification mode of a wide range of Fe-Cr-Ni-Mo alloys that simulate the compositions of SASS alloys. Alloys above and to the left of the eutectic line should exhibit primary austenite solidification, while compositions below and to the right of this line will exhibit primary ferrite solidification. Alloy compositions that solidify as primary ferrite and exhibit the thermodynamic potential to experience a solid-state transformation to the austenite phase during cooling can also be identified in the diagrams. Compositions above and to the left of the maximum solubility of Cr in austenite should experience solid-state transformation to austenite, as the composition may now enter the single-phase austenite region of the phase diagram. Compositions below and to the right may also experience solid state transformations by entering the  $\delta + \gamma$  two-phase regions. Because  $\delta$  is still thermodynamically stable in these alloys, the  $\delta \rightarrow \gamma$  transformation will not proceed to completion. Since the diagrams take into account only thermodynamic considerations, they are not proficient at predicting the type or amount of transformation that will occur. This factor can only be found through an analysis of the kinetics of the system, which takes into account the cooling conditions present. Therefore, the diagrams represent a necessary, but not sufficient, condition for attaining a fully-austenitic alloy derived by ferritic solidification.

### 1.3.2 Model Validation and Microstructural Characterization

The results of microstructural characterization of the alloy matrix showed a wide variety of microstructural development sequences and morphologies. A third of the samples showed evidence of the martensite phase. Good agreement was shown between the compositions of martensite-containing samples and those predicted by the Schaeffler Diagram. Microstructural analysis and determination of the solidification mode of these alloys was not conducted, in order to maintain focus on alloys composed predominately of austenite. The four solidification modes present in the remaining 64 alloys, in order of increasing Cr/Ni content, were austenitic (A), austenitic-ferritic (AF), ferritic-austenitic (FA), and ferritic (F). The order of phases listed for the dual-phase modes represents the order of solidification. The solidification modes and ferrite contents of all samples are given in Table I. In addition to the four solidification modes, the arc-melt structures exhibited three different solid-state phase transformations: the diffusional transformation  $\delta \rightarrow \gamma$ , the eutectoid transformation  $\delta \rightarrow \gamma + \sigma$ , and the shear transformation

$\gamma \rightarrow$ martensite. The twenty possible phase transformation sequences are listed in Table II. All compositions that contained solidified ferrite exhibited the  $\delta \rightarrow \gamma$  transformation, although the particular mechanism varied depending on the solidification mode. The eutectoid transformation to  $\sigma$ -phase will be discussed separately below.

**Table II. The twenty microstructural development sequences found to result in Fe-Ni-Cr-Mo alloys from the arc-melt condition.**

Solidification Mode	Solidification sequence	Primary Transformation	Secondary Transformations	Final microstructure
A	$L \rightarrow L + \gamma_p \rightarrow \gamma_p$	—	—	$\gamma_p$
			$\gamma_p \rightarrow M$	$\gamma_p + M$
			$\gamma_p \rightarrow \gamma' + \sigma_{prec}$	$\gamma_p + \gamma' + \sigma_{prec}$
			both	$\gamma_p + \gamma' + \sigma_{prec} + M$
AF	$L \rightarrow L + \gamma_p \rightarrow L + \gamma_p + (\delta/\gamma)_e \rightarrow \gamma_p + (\delta/\gamma)_e$	$\delta_e \rightarrow \gamma_{tf}$	—	$\gamma_p + \gamma_e + \gamma_{tf}$
			—	$\gamma_p + \gamma_e + \delta_e + \gamma_{tf}$
			$\gamma_p \rightarrow M$	$\gamma_p + \gamma_e + \gamma_{tf} + M$
			$\gamma_p \rightarrow M$	$\gamma_p + \gamma_e + \delta_e + \gamma_{tf} + M$
			$\delta_e \rightarrow (\gamma/\sigma)_{eutectoid}$	$\gamma_p + \gamma_e + \gamma_{tf} + (\gamma/\sigma)_{eutectoid}$
			$\delta_e \rightarrow (\gamma/\sigma)_{eutectoid}$	$\gamma_p + \gamma_e + \delta_e + \gamma_{tf} + (\gamma/\sigma)_{eutectoid}$
			both	$\gamma_p + \gamma_e + \gamma_{tf} + (\gamma/\sigma)_{eutectoid} + M$
			both	$\gamma_p + \gamma_e + \delta_e + \gamma_{tf} + (\gamma/\sigma)_{eutectoid} + M$
FA	$L \rightarrow L + \delta_p \rightarrow L + \delta_p + (\delta/\gamma)_e \rightarrow \delta_p + (\delta/\gamma)_e$	$\delta_p, \delta_e \rightarrow \gamma_{tf}$	—	$\delta_p + \gamma_e + \gamma_{tf}$
			$\gamma_e, \gamma_{tf} \rightarrow M$	$\delta_p + \gamma_e + \gamma_{tf} + M$
			$\delta_p \rightarrow (\gamma/\sigma)_{eutectoid}$	$\delta_p + \gamma_e + \gamma_{tf} + (\gamma + \sigma)_{eutectoid}$
			both	$\delta_p + \gamma_e + \gamma_{tf} + (\gamma + \sigma)_{eutectoid} + M$
F	$L \rightarrow L + \delta_p \rightarrow \delta_p$	$\delta_p \rightarrow \gamma_{gb} + \gamma_{Wid}$	—	$\delta_p + \gamma_{gb} + \gamma_{Wid}$
			$\gamma_{gb} + \gamma_{Wid} \rightarrow M$	$\delta_p + \gamma_{gb} + \gamma_{Wid} + M$
			$\delta_p \rightarrow (\gamma/\sigma)_{eutectoid}$	$\delta_p + \gamma_{gb} + \gamma_{Wid} + (\gamma + \sigma)_{eutectoid}$
			both	$\delta_p + \gamma_{gb} + \gamma_{Wid} + (\gamma + \sigma)_{eutectoid} + M$

L = liquid;  $\gamma$  = austenite phase;  $\delta$  = ferrite phase;  $\sigma$  = sigma phase; M = martensite;  
 $p$  = primary solidification product;  $\gamma'$  = phase of reduced concentration; prec = phase created by precipitation; e = eutectic solidification product; tf = product of long-range diffusional solid-state phase transformation; eutectoid = product of eutectoid phase transformation; gb = grain-boundary allotriomorph; Wid = Widmanstatten platelets.

While both the FA and F solidification modes follow the prescribed two-stage development sequence, the FA mode alloys were shown to contain much less ferrite phase at room temperature. During cooling, the austenite formed at the end of solidification served as an effective nucleus for the solid-state transformation of the primary ferrite into austenite. Therefore, the transformation was far more efficient at eliminating the ferrite component of the microstructure than in F alloys. Ferrite readings from the FA alloys displayed low (~5wt%) ferrite contents, showing that the solid-state transformation to austenite was successful at consuming nearly all of the primary solidified ferrite. EBSD analysis confirmed the identity of the austenite and ferrite components of the microstructures, which were in accordance with previously published data.

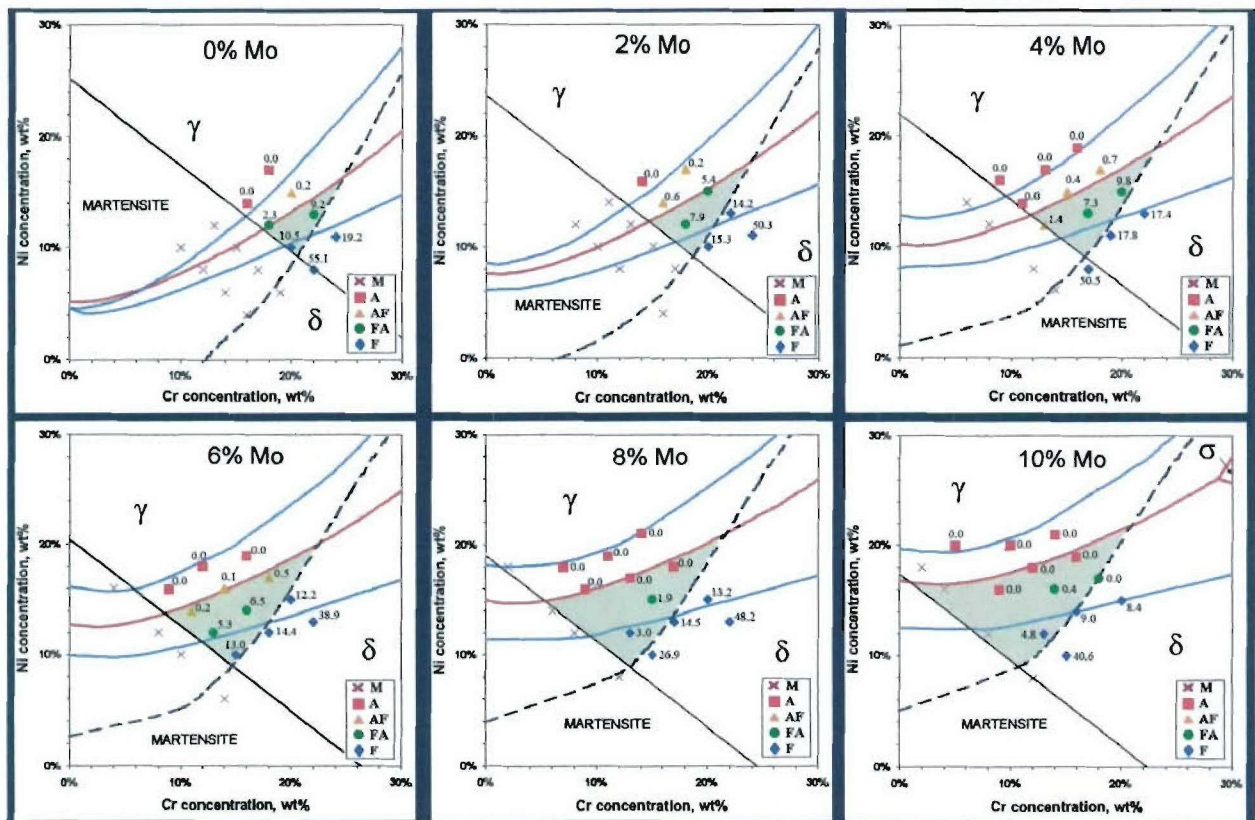


Figure 3. Phase stability diagram for all Mo contents. Each data point represents the nominal alloy compositions. The shape and color of each data point represents the solidification mode, while the adjacent values represent its wt% ferrite. Data points marked 'M' represent alloys that contained martensite.

The phase stability diagrams detailed in the previous section were validated using the experimental alloys. The compositions of alloy buttons were plotted by their nominal Cr and Ni contents on the phase stability diagram of the corresponding Mo content, as shown, for all compositions studied, in Figure 3. The data point locations represent alloy compositions, and the corresponding values represent the weight percentages of ferrite. The calculated eutectic lines were fairly accurate in separating alloys between the austenitic and ferritic primary solidification modes, especially in the lower Mo diagrams. Of the 64 alloys that contained no martensite, only eight were found to disagree with the solidification modes predicted by the phase stability diagrams. In nearly all cases, their nominal compositions were very close to the calculated eutectic lines. Most importantly, all compositions that experienced the desired two-step development sequence were found between the computed boundaries of the diagram predicting their existence. As shown by the round, green data points in Figure 6, a number of promising alloy compositions were identified that exhibited the desired FA solidification mode and very low ferrite contents.

### 1.3.3 Sigma Phase

In addition to the ferrite-to-austenite transformation, a second solid-state transformation was observed in alloys of high Mo content. Both primary solidified ferrite and intercellular ferrite were shown to exhibit a eutectoid transformation of the form  $\delta \rightarrow \gamma + \sigma$ . Although  $\sigma$ -phase is commonly found in stainless steels as a solidification product, evidence showed the  $\sigma$ -phase to be a product of solid-state transformation. The location of  $\sigma$ -phase at the dendrite cores of FA mode alloys and between Widmanstatten platelets in F mode alloys established that the  $\sigma$ -phase must have formed after the  $\delta \rightarrow \gamma$  transformation. The effect of this transformation was to further eliminate traces of residual ferrite, as shown by the low ferrite readings for higher-Mo alloys in Table I. While this could initially be construed as an advantageous reaction for eliminating the magnetic signature in the weld zone, the properties of the  $\sigma$ -phase are detrimental to the mechanical properties of the weld. Microstructural observations showed that the presence of  $\sigma$ -phase can be predicted based on the composition of the weld. Plotting the alloys based on their  $\text{Cr}_{\text{eq}}/\text{Ni}$  ratio and Mo content shows a distinct region of  $\sigma$ -containing compositions. Figure 4 displays a map of all alloys based on these two parameters. Each data point represents an alloy

composition, where the form of the data point is representative of the solidification mode and the presence of  $\sigma$ -phase. The map not only predicts the presence of  $\sigma$ -phase, but also exhibits well-defined compositional boundaries between solidification modes. A boundary exists at a  $\text{Cr}_{\text{eq}}/\text{Ni}$  ratio of 1.5 that clearly separates the ferritic and austenitic solidification modes, whereas a boundary at 1.7 separates FA mode and F mode alloys. Another advantage of the FA solidification mode is demonstrated by this map: up to 6wt% Mo may be held by an FA mode alloy without production of  $\sigma$ -phase via solid-state transformation. Alloys containing 4-6wt% Mo that solidified primarily as austenite (AF mode) showed evidence of the  $\sigma$ -phase, while alloys of similar composition on the opposite side of the eutectic (FA mode) did not.

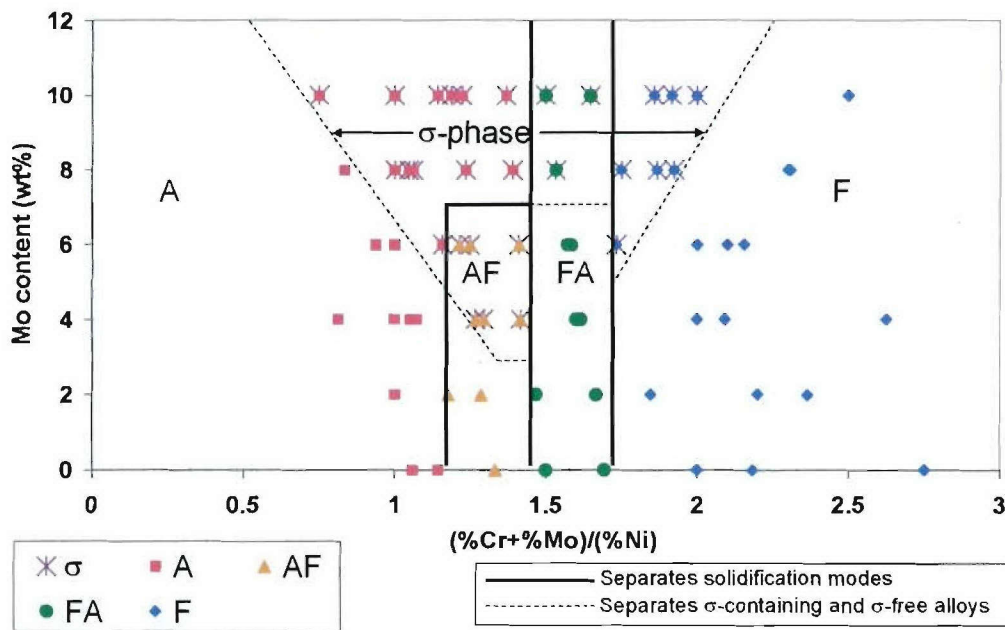


**Figure 4. The effect of  $\text{Cr}_{\text{eq}}/\text{Ni}$  ratio and Mo content on solidification mode and presence of  $\sigma$ -phase.**

#### 1.3.4 Solute Distribution

Electron Probe Micro-Analysis (EPMA) was performed on a subset of alloys in order to examine the distribution of solute elements within each type of microstructure. An example of the difference in solute profiles between the microstructures of AF and FA solidification modes for the 10wt% Mo system are shown in Figure 5. The Mo profile shows a definite increase in concentration in the distance between a cell core and the neighboring intercellular region

produced by AF solidification. This was caused by the solidifying cell rejecting Mo into the liquid. The solute accumulates in the intercellular region, since it is the last to solidify. A similar process occurs in the solidification of ferrite, with solute being rejected to the liquid. Owing to the improved diffusivity of solute in the open bcc structure of ferrite, the excess Mo in the intercellular region is able to diffuse down the concentration gradient towards the cell core. The regions of austenite formed by solid-state transformation in Figure 5b show a more uniform concentration of Mo. Since the central axis of the austenite regions represents the former intercellular regions of the solidified ferrite cells, it is established that the initial concentration gradient of Mo was significantly reduced via backdiffusion. For example, the AF alloy had a nominal Mo concentration of 9.9 wt%, but the dendrite cores contain only 6 wt% Mo. In contrast, the FA alloy had a nominal Mo concentration of 9.8 wt%, and the dendrite cores are very close to this value at 8.5 wt%. Some of the Mo is partitioned to the neighboring residual ferrite, which accounts for the slightly lower core value. However, note that the Mo distribution in the austenite obtained through the FA solidification mode is significantly more uniform than that obtained by the AF mode. This should provide a significant improvement in corrosion resistance.

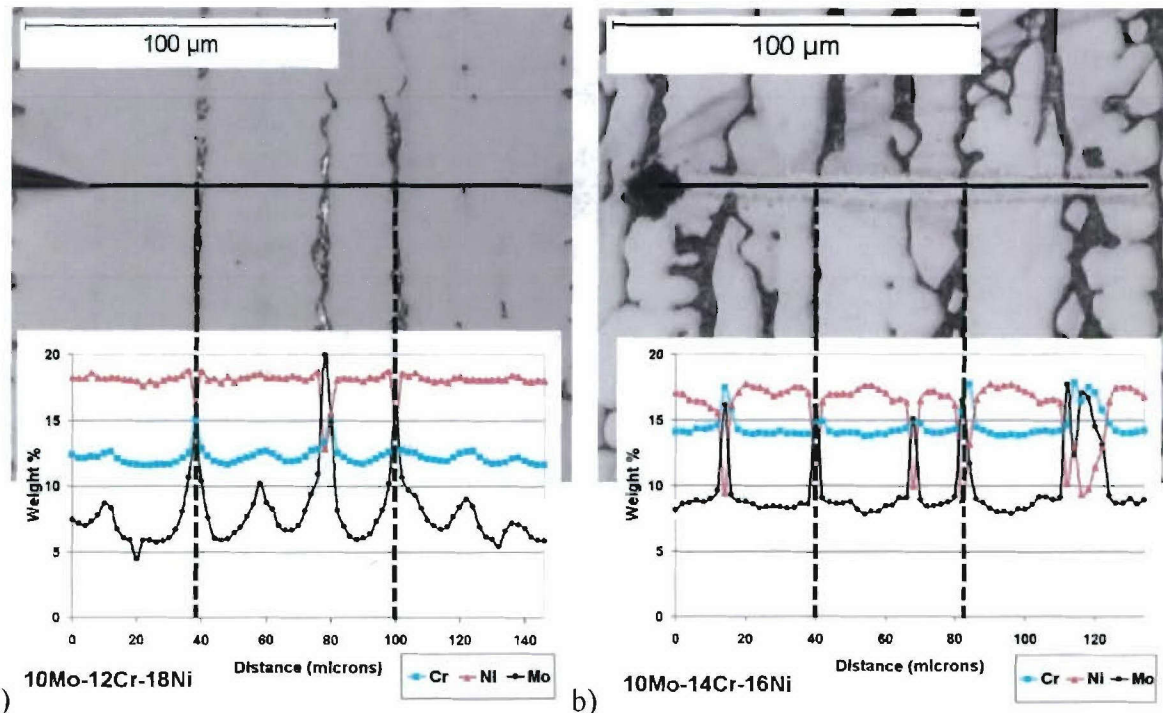


**Figure 5. EPMA line scan data for microstructures with austenite (light phase) derived by a) solidification (AF mode), and b) solid-state transformation (FA mode).**

### *1.3.5 Higher-Order Alloys*

Work is currently being conducted at Lehigh to explore the effects of additional alloying elements on the microstructural development behavior of this alloy system. Commercial alloys can include upwards of ten elements, the concentrations of which are carefully controlled for specific properties and alloy behavior. Research must therefore be done to ascertain the effects of further elements on the FA solidification zone and potentially identify alloy additions that can completely eliminate residual ferrite from the microstructure. Thermodynamic calculations have been performed and phase stability diagrams have been constructed that include the effects of the alloying elements C, N, Mn, W, Si, V, Nb, Ti, and Co. In all cases, the zone of desired FA solidification is altered, either in size or location. Phase stability maps of the 6wt% Mo condition are provided in the appendix that detail the effects of each individual element on the range of compositions that may experience the two-stage development sequence prescribed in this research. Colored fields are superimposed on the familiar phase stability diagram representing the FA zone with the new solute added. Blue represents the addition of 2wt%, and red represents 4wt%. The exceptions to this are carbon (0.01, 0.02wt%) and nitrogen (0.1, 0.2wt%). In each map, the span of acceptable compositions of AL-6XN is included in the form of a pink box. This location is an important consideration: the closer it lies to the zone of FA compositions, the more weld dilutions will be possible.

The addition of nitrogen or cobalt will drive the zone to higher Cr and lower Ni contents. The effect is detrimental, since this action drives the range of available compositions further from the composition of AL-6XN. Vanadium and silicon will have the opposite effect, pushing the FA zone to higher Ni and lower Cr contents. This could be helpful, but in the case of vanadium, the width of the zone is significantly reduced. The addition of titanium, tungsten, or niobium also appears to truncate the width of the FA zone by drawing the eutectic line and maximum solid solubility line together. Carbon and manganese do not appear to alter the location or width of the FA zone. Adding manganese or silicon will suppress the martensite boundary to lower Cr and Ni compositions. While this effect does enhance the range of possible compositions (and thus dilutions), the newly available Cr concentrations are undesirable from a corrosion resistance standpoint.

From these observations, it was determined Si and Mn were the solute additions with the greatest potential for expanding the range of possible dilutions for welding with super-austenitic

stainless steel. A matrix of phase stability diagrams were completed using incremental additions of Si and Mn at various combinations of 2 and 4wt% of each. While the width of the zone was shown to decrease slightly, the location of the zone was brought slightly closer to the composition of the proposed base metal, AL-6XN. Each diagram was then evaluated by estimating the range of dilutions that would be available to any filler metal composition within the FA microstructural development zone. This estimation was made using the assumption that a line drawn between the candidate filler metal composition and the nominal composition of AL-6XN would describe all possible compositions that would result from mixing, from 0 to 100% dilution. Welds consisting mostly of base metal are close to 100% dilution, while filler-metal rich welds are near the 0% dilution limit. The eutectic line represents the limit of dilutions that will still fall within the FA zone. The length of the tie-line between the two filler and base metal compositions and the distance between the filler metal composition and the eutectic line are measured. The ratio of these two measurements is taken to be equal to the maximum range of dilutions possible from welds using that particular filler metal. This calculation is only made possible with the assumption that the filler and base metals contain exactly the same Mo content of 6wt%. This procedure was enacted for all whole-number combinations of Cr and Ni within the FA zone. The resulting contour map, such as that shown below in Figure 6, describes the range of dilutions possible for the entire FA zone. The boundaries of this range describe the eutectic line, the maximum solubility of Cr in austenite, and the martensite boundary in the same configuration as in the phase stability diagrams. The Z direction (height) in this figure describes the maximum dilution level possible at each point. These values are described using color-coded zones divided into increments of 10%.

Compositions furthest from AL-6XN showed the highest possible dilutions, since their tie-lines encompassed most of the FA zone. The addition of Mn and Si was shown to drive the maximum possible dilution from 54% up to 75%. The process by which these numbers were evaluated showed that the actual width of the FA zone was not particularly relevant when determining the efficacy of a candidate filler metal. Rather, it implies that greater precision will be required in the construction of the filler metal so that its composition is within the range. With this obstacle overcome, the diluted compositions will all lie along the tie-line, which has been shown to reside by and large within the FA zone.

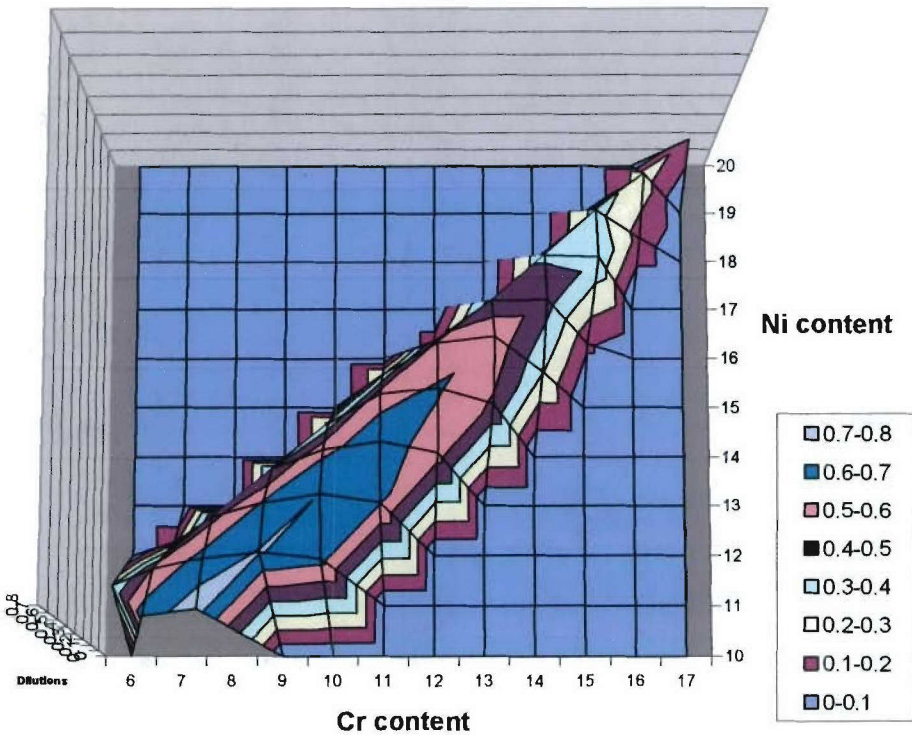


**Figure 6.** Dilution calculations for stainless steel alloys containing 6wt% Mo, 2wt% Mn, and 4wt% Si. The color-coded regions denote the maximum possible dilutions available for a candidate filler metal of such a composition.

The calculations described detail only the possible development behavior for these alloys based on thermodynamics. The actual microstructures that develop will also be based on the kinetics of the newly introduced solute atoms. Experiments will be required that will seek to determine what, if any, are the effect of these additional elements on the progression of the  $\delta \rightarrow \gamma$  solid-state transformation and concomitant amount of residual ferrite. Mn- and Si-bearing alloy buttons will be melted of the prescribed compositions shown in Table III. This sample will represent the filler metal composition. Parts of each button will then be diluted with pieces of AL-6XN to represent compositions that would result from using this filler metal with the SASS base metal. Microstructural characterization and EPMA analysis will then be carried out on all samples for comparison with the results presented herein for Fe-Ni-Cr-Mo alloys. This work will be completed under the current ONR grant.

**Table III.** The maximum possible dilutions found for each combination of Mn and Si addition.

Mn	Si	Cr	Ni	Dilutions
0	0	0.15	0.1	0.54
0	2	0.13	0.1	0.62
0	4	0.12	0.13	0.69
2	0	0.15	0.1	0.55
2	2	0.12	0.08	0.68
2	4	0.08	0.1	0.75
4	0	0.14	0.08	0.63
4	2	0.12	0.08	0.70
4	4	7	10	0.73

### 1.3.6 HED Welds

The elevated cooling conditions present in the HED weld zones were found to incur considerable modifications to the microstructural development. The elliptical shape of the ripples observed on the weld surface implied that the maximum solidification velocity in each weld was equal to the travel speed of the laser. Based on dendritic measurements, the cooling rates present in these welds were found to range from  $10^4$  to  $10^5$  °C/s, in comparison to the cooling rate of  $\sim 20$  °C/s in the melt buttons. Each of the four solidification modes observed in the melt button samples were found in the laser welds. The presence of  $\sigma$ -phase was shown to be severely reduced in the HED welds of alloys that contained significant amounts of  $\sigma$ -phase in the arc-melt structure. The high cooling rates produced in these regions did not supply the necessary time for Mo to diffuse and nucleate  $\sigma$ -phase. More importantly, though, microstructural characterization revealed a subset of the weld structures that was found to experience a new variant of the ferrite-to-austenite conversion: the massive transformation.

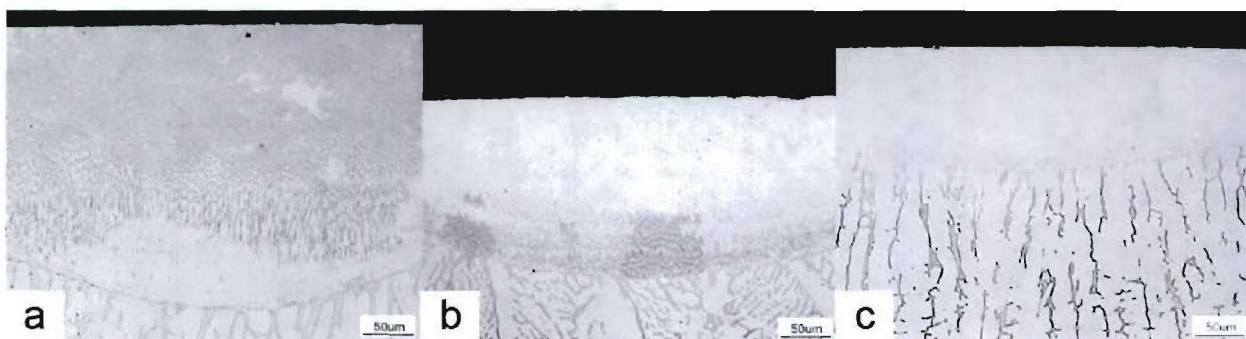


**Figure 7.** Examples of massive  $\gamma$ -austenite morphology for laser welds prepared on FA mode alloy 2Mo18Cr12Ni. Note the increase of massive product as the solidification velocity, and thus cooling rate, are increased from: a) 4.2mm/s; b) 21 mm/s ; c) 42 mm/s.

The massive type of transformation is known to occur specifically at high cooling rates where other diffusional transformation mechanisms are suppressed. The massive interface between parent and product phases moves at such high velocities that diffusion only occurs across the interface and not within the matrix of the parent phase. The resulting austenitic product thus inherits the chemical distribution of the parent ferrite phase. The compositional invariance of the massive transformation can thus allow an austenite structure to exhibit the uniform concentrations of Mo typical of the ferrite phase.

The massive transformation was seen in both laser welds conducted on both F and FA solidification mode alloys, where a driving force existed to transform to austenite. The process was observed predominately in FA mode alloys. This detail is explained by the greater driving force for transformation previously displayed in the arc-melt condition. In addition, nucleation was not required in these alloys, since intercellular austenite was available from which epitaxial growth could occur. A patchy morphology with irregular grain boundaries, as shown in Figure 7 and Figure 8, was characteristic of the massive product; positive phase identification using EBSD confirmed that this was indeed the austenite phase. The massive transformation was observed to go further to completion with increasing solidification velocity, illustrating the significant effect of cooling rate on this mechanism. Figure 7 shows micrographs of laser welds of alloy 2Mo18Cr17Ni that typify this behavior.

EPMA analyses were also performed on laser welds containing this patchy morphology. As shown by example in

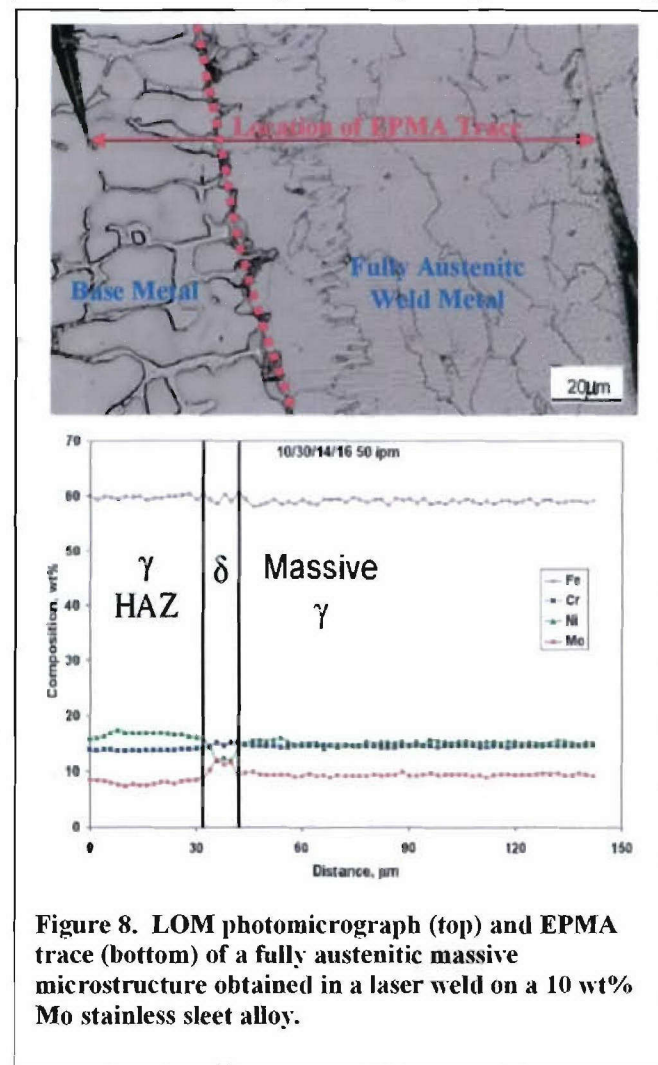


**Figure 8.** LOM photomicrograph (top) and EPMA trace (bottom) of a fully austenitic massive microstructure obtained in a laser weld on a 10 wt% Mo stainless steel alloy.

Figure 8, the massive product displays a uniform distribution of all alloying elements. This data matches similar results measured from fully-ferritic weld zones in other alloys. It can thus be concluded that the hallmark composition-invariant nature of the massive transformation is present in these alloys. The uniform Mo concentrations present in the massive structures should supply them with a corrosion resistance superior to any as-solidified austenitic structure of comparable composition. The segregation-free, fully-austenitic structure will also exhibit no magnetic signature and provide excellent toughness.

Thermodynamic analysis was performed in order to determine the controlling parameter for the massive transformation to ensue. At the focus of these studies was a temperature value  $T_o$ , which is the temperature within the two-phase region in which the chemical potential of each phase ( $\delta$  and  $\gamma$ ) is equal. It has been well-established<sup>10</sup> that the alloy must be quenched below this value prior to completion of the  $\delta \rightarrow \gamma$  long range diffusional transformation in order for the massive transformation to occur. What is not known is whether or not the controlling factor is the relative magnitude of  $T_o$ , or whether it is the magnitude of the difference between  $T_o$  and the  $\delta$  solvsus temperature,  $\Delta T_o$ . These values are shown schematically in Figure 9. Higher values of  $T_o$  and lower values of  $\Delta T_o$  are preferable for massive growth to take place. Further studies conducted on strategically selected alloy compositions could assist in separating these effects.

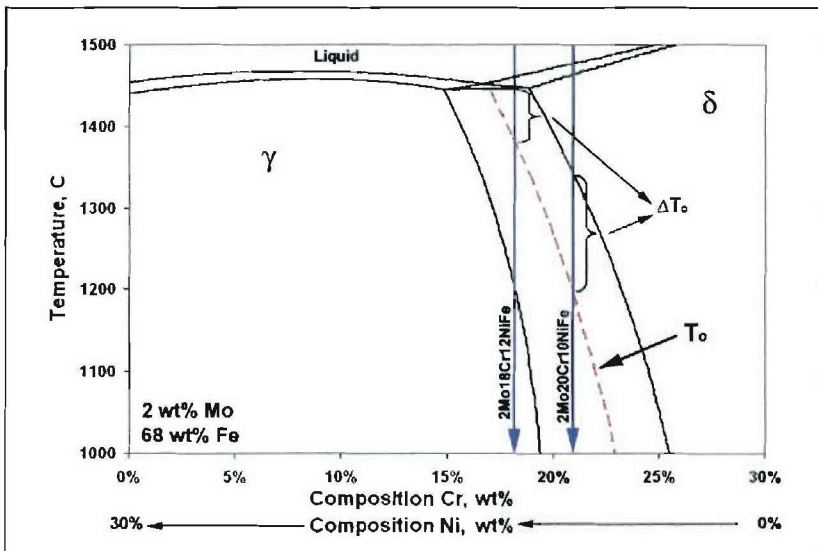


**Figure 9.** Calculated vertical phase diagram for constant additions of 2 wt% Mo, 68 wt% Fe. The significance of  $T_o$  and  $\Delta T_o$  are shown for FA mode alloy 2Mo18Cr12Ni and F mode alloy 2Mo20Cr10Ni.

This information would be useful as it could then be used to control processing parameters for development of the massive microstructure.

## 2. Mechanical Behavior Research

### 2.1 *Background*

The presence of  $\sigma$ -phase particles in AL-6XN plate material, particularly arranged in microstructural bands or packets containing high volume fractions of the particles at and surrounding the centerline of the plate, as seen in Figure 10, has been shown to be unfavorable. For example, previous experiments at Lehigh University involving fillet welding and fatigue loading of this material caused the base-plate to split along its centerline. Subsequent failure analysis<sup>12</sup> showed that the fracture occurred as cracking within regions of high  $\sigma$ -phase particle content and propagated along Cr-oxide stringers. Moreover, any tensile stresses that act upon this material, perpendicularly to the plane of the plate, can be expected to present similarly adverse effects, provided it contains some form of metallurgical imperfections or stringers as previously mentioned. Thus, the impetus for this work is to ascertain the effects of the brittle  $\sigma$ -phase particles, which are arranged in areas of high-density, on the through-thickness (short-transverse [S-T]) mechanical properties of this material.

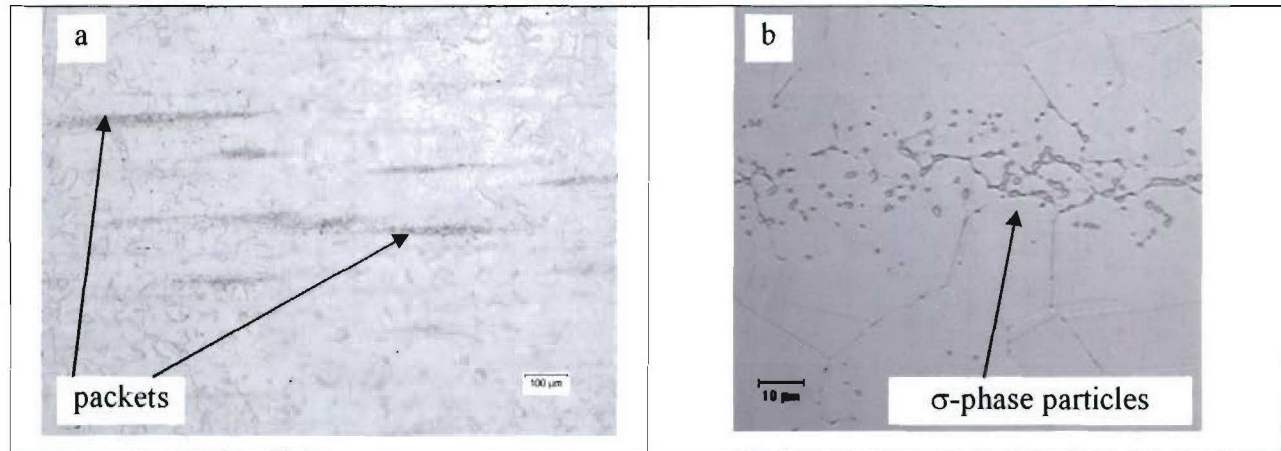


**Figure 10.** Light optical micrographs of metallographically prepared transverse cross-sections of 25.4-mm-thick AL-6XN plate material, (a) exhibiting the ‘packet’ morphology of  $\sigma$ -phase particles within the matrix austenite grain structure parallel to the centerline of the plate and (b) showing the appearance of the particles that make up the packets.

## 2.2 Experimental Procedure

The AL-6XN material used in this study includes 25.4-mm-thick plate material for testing in the through-thickness (S-T) orientation and 15.9-mm-thick plate for testing in the longitudinal and transverse rolling directions (RD) (T-L and L-T, respectively). To obtain material considered to be ‘ $\sigma$ -phase or packet-free,’ material was cut approximately 7.5-8.0-mm from the surface of the 25.4-mm-thick plate material, since  $\sigma$ -phase packets were nominally absent in this region. The compositions of these plates are shown in Table IV. To observe the microstructure of the material, specimens were electrolytically etched using a solution of 60% HNO<sub>3</sub> and 40% H<sub>2</sub>O with a potential of 2.5-3.0 V in 10 second intervals using a Pt electrode.

**Table IV. Composition of 25.4-mm-thick and 15.9-mm-thick AL-6XN plate material**

Element (wt%)	25.4-mm-thick plate	15.9-mm-thick plate
C	0.02	0.02
Mn	0.51	0.38
P	0.016	0.016
S	0.001	0.001
Si	0.46	0.50
Cr	20.54	20.69
Ni	24.31	24.06
Mo	6.01	6.11
N	0.22	0.22
Cu	0.19	0.20
Co	0.12	0.11
Fe	47.60	47.69

Testing of the through-thickness mechanical properties of the as-received material was achieved by electron-beam welding extensions of AL-6XN plate material to the surface. This was done in order to fabricate standard, full-size specimens, see Figure 11. The electron-beam welding was conducted at Los Alamos National Laboratory, using the following process parameters: 110 kV, 15-23 mA, and 10-15 ipm (inches per minute, travel speed).

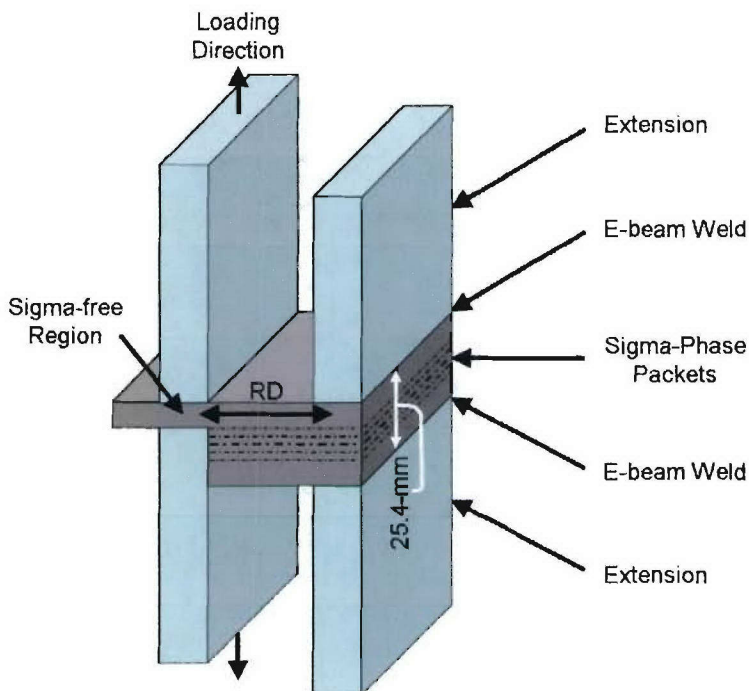


**Figure 11.** Schematic representation of how the samples were obtained in the through-thickness (short-transverse) direction. The rolling direction (RD) of the through-thickness section is indicated.

Tensile testing ‘dog-bone’ specimens were fabricated in accordance with ASTM E-8-04<sup>13</sup>, “Standard Test Methods for Tension Testing of Metallic Materials,” however, they contained two electron-beam welds within the reduced cross-sectional area of the samples. From preliminary tests, the need arose to introduce a second reduced cross-sectional area between the welds, having a gauge-length and width each of 6.35-mm, in order to concentrate all deformation within the through-thickness zone, see Figure 12. This came about as a result of premature failure at the electron-beam welds in the  $\sigma$ -free samples, which was not within the section of interest. The gauge-length was consistent for both  $\sigma$ -containing and  $\sigma$ -free samples to avoid additional test variables. Longitudinal and transverse orientations were not tested since a similar study had been done previously<sup>14</sup>. A 12.7-mm extensometer was used for strain measurements and the final elongation measurements were made using original gauge-length marks 6.35-mm apart. The yield strength was determined using the 0.2%-offset method with a cross-head speed of 0.508-mm/sec. A 5.08-mm/sec cross-head speed was used to reach final fracture.

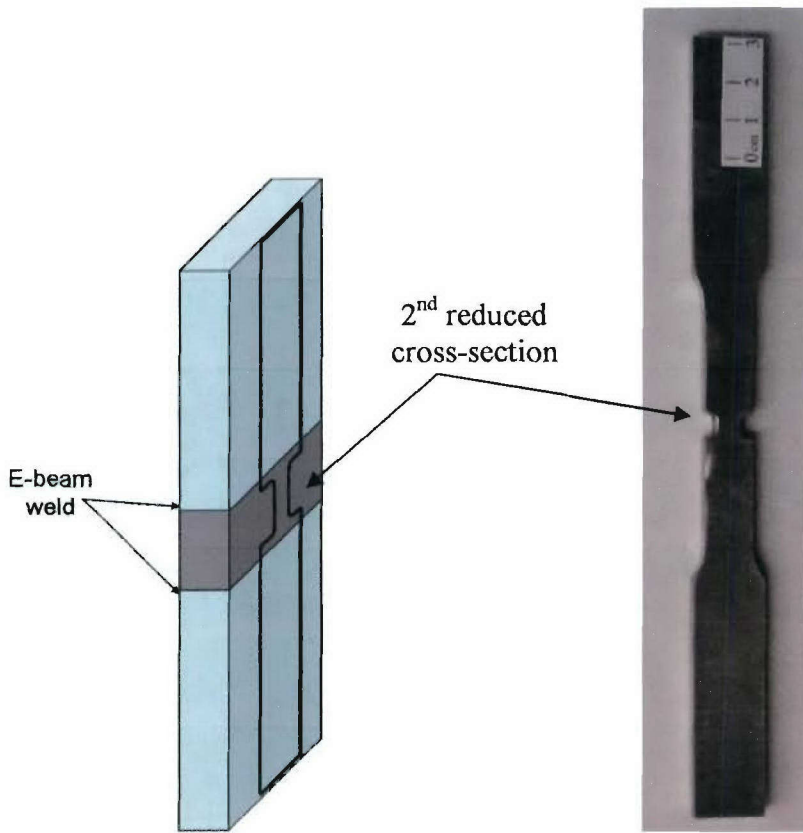


**Figure 12. Tensile sample orientation, showing gauge length within central plate material.**

Standard compact tension (C(T)) specimens were fabricated for both fracture toughness and fatigue testing having 12.7-mm-thicknesses and 50.8-mm-widths (measured from the load-line to the end of the specimen), see Figure 13. Specific geometries were consistent with the respective ASTM standards for each test type. Single-specimen fracture toughness testing was carried out in accordance with ASTM E-1820-05<sup>15</sup>, “Standard Test Method for Measurement of Fracture Toughness.” The tests were performed using an MTS-brand 100 kN servo-hydraulic uniaxial loading system and a MTS 458 controller, which used an integrated “Adwin-Gold FTA” computer to analyze the raw data for fracture toughness calculations and to report various information. R-curves ( $J-\Delta a$ ), representation of a material’s resistance to crack extension, were generated for each specimen condition: S-T (with and without  $\sigma$ -packets), L-T, and T-L.  $J$  was used instead of  $K$  as a fracture criterion since the sample size requirements for valid  $K_{IC}$  testing as noted in ASTM E-399<sup>16</sup> would require an unusually large sample. For a valid plane-strain fracture toughness  $K_{IC}$  test, the  $\sigma_y/E$  ratio for AL6XN would require a nominal specimen thickness much greater than 7.62cm, which was not feasible due to fabrication limitations.  $J$ -

testing allowed the use of the 12.7-mm thickness for the samples, which was well within range for the electron-beam welding process used. Light optical microscopy (LOM) and scanning electron microscopy (SEM) techniques were used to characterize how the microstructure of the material influenced or was influenced by the test.

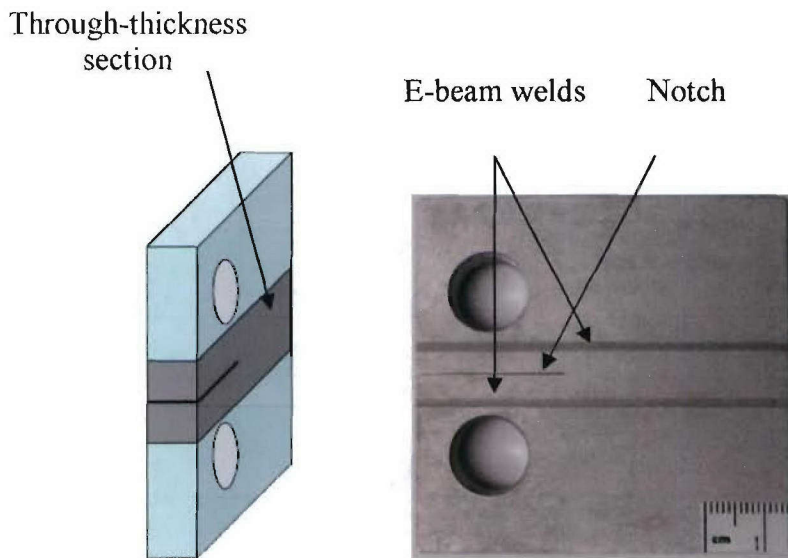


**Figure 13. Compact tension specimen for fatigue testing showing geometry with notch parallel to centerline of central plate material. The sigma-free sample shown on the right was macroetched to reveal the location of the electron beam welds.**

Fatigue tests were carried out in accordance with ASTM E-647<sup>17</sup>, “Standard Test Method for Measurement of Fatigue Crack Growth Rates.” The tests were performed using an Instron-brand 24.5 kN servo-hydraulic uniaxial loading system and a MTS clip gauge, all interfaced with a PC using Fracture Technology Associates, Inc. software (version 2.53) to compute the fatigue crack growth data using the loads applied and compliance-based crack length measurements. The tests were conducted using constant amplitude loading with a sine wave-form at a frequency of 24Hz, all at room temperature and laboratory air conditions. A constant stress-ratio  $R = 0.6$ <sup>18</sup> and K-gradient control of the applied stress-intensity factor were used to obtain the fatigue curves. To account for crack closure, the effective  $\Delta K$  experienced by the crack tip was calculated using the 2/pi method<sup>19</sup>. Additionally, tests were conducted on selected samples using the ACR (adjusted compliance ratio) method<sup>20</sup> to verify the results.

Light optical microscopy (LOM) and scanning electron microscopy (SEM) techniques were used to characterize how the microstructure of the material was influenced by the test. Olympus BH-2 and Nikon light microscopes were used in conjunction with PAXit software

interfaced with PAXcam2 cameras to collect photomicrographs. A Philips XL30 scanning electron microscope, using accelerating voltages ranging between 10 – 20 kV depending on optimal configuration for acquiring images or collecting x-rays from the specimens, was also used to collect photomicrographs.

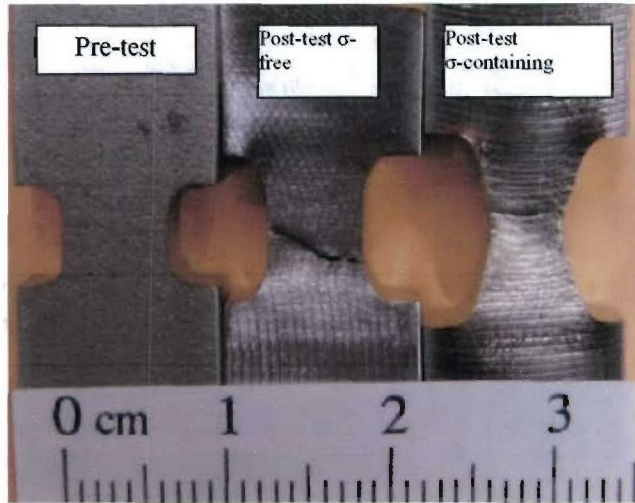
## **2.2 Results and Discussion**

### **2.2.1 Tensile Testing**

Table V shows the tensile data for the S-T( $\sigma$ ) and S-T( $\sigma$ -free) sample orientations. The  $\sigma$ -free samples show remarkably greater strength and ductility compared to the  $\sigma$ -containing samples. The variation in the tensile data seen for the  $\sigma$ -containing samples is an indication of the degrading effects of the presence of sigma-phase particles in microstructural packets since fracture occurred at various strains. The reduction of the yield and tensile strengths when the  $\sigma$ -phase packets are present could be due to cracking of the  $\sigma$ -particles, causing premature fracture of the matrix, not allowing it to work-harden as much as it would otherwise. The macroscopic post-test appearance and cross-section view of the samples (Figure 14), which show, first-hand, much more plastic deformation for the sigma-free sample, is a significant example of how the presence of these  $\sigma$ -phase packets affect the tensile properties of this alloy.

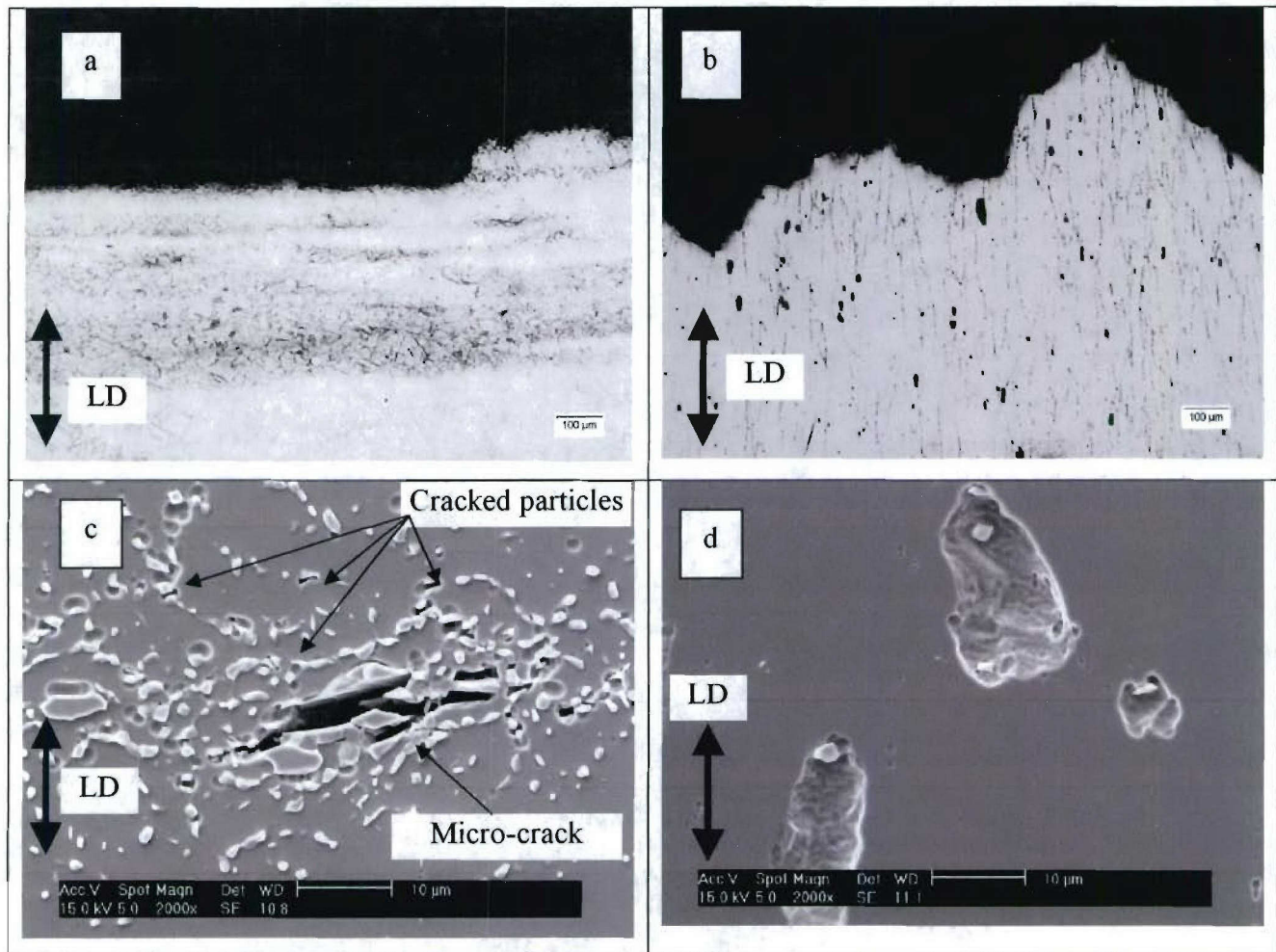
**Table V. Tensile data for the two through-thickness conditions:  $\sigma$ -sigma-containing and  $\sigma$ -sigma-free**

Sample	Tensile Strength (MPa)	Yield Strength (MPa)	Elongation (%)	Reduction in Area (%)
Sigma-containing	793	421	38	28
Sigma-containing	569	455	12	10
Sigma-free	862	497	76	65
Sigma-free	855	486	79	65



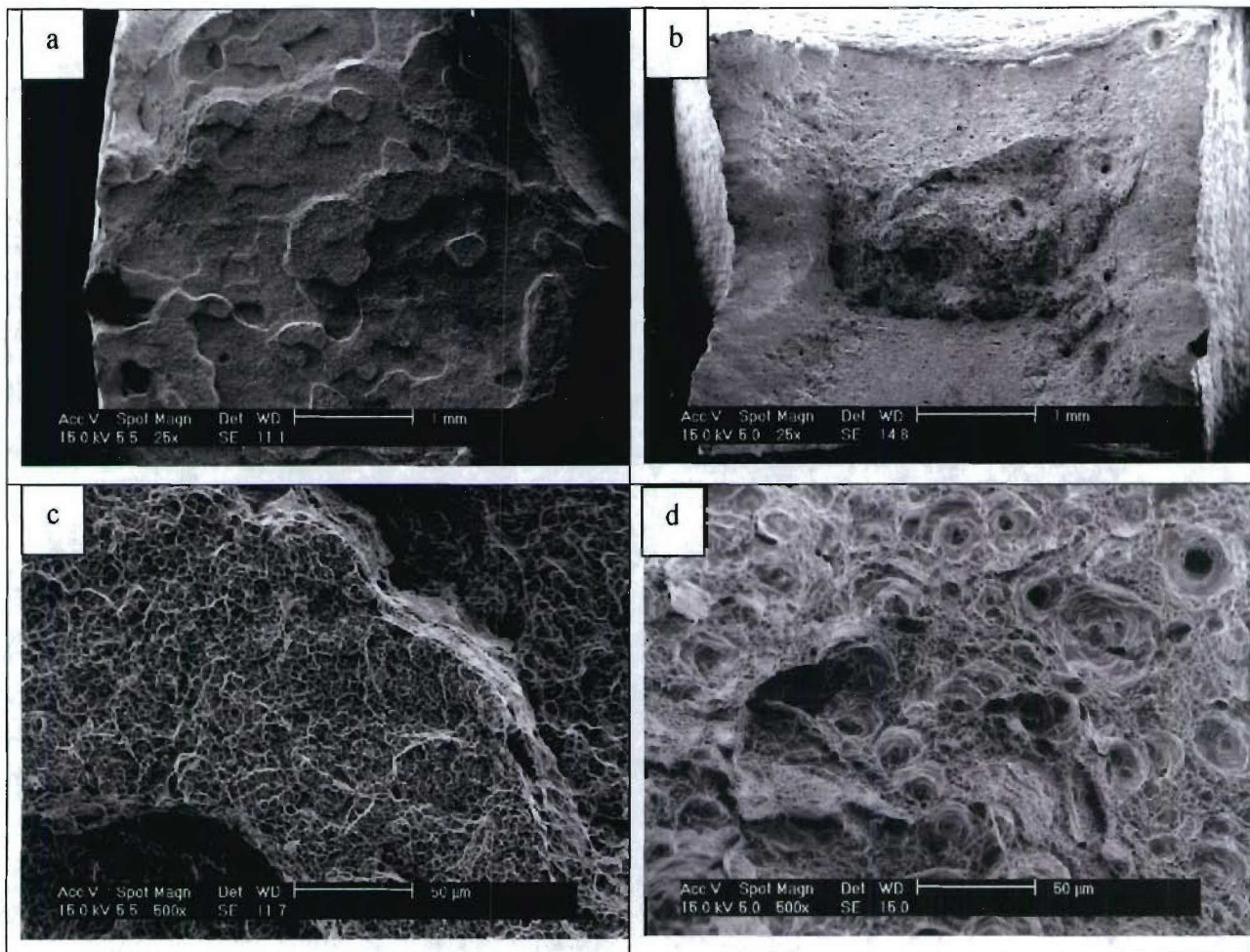
**Figure 14.** Pre-test view of the original sample dimensions and post-test views of the two tensile sample orientations; the sigma-free sample shows remarkably more plastic deformation.

Figure 15a and b represent longitudinal cross-sections through a portion of the gauge length, up to and including the final fracture surface, for the two sample orientations tested ( $S-T(\sigma)$  and  $S-T(\sigma\text{-free})$ ). Since the tensile bars had fractured, creating two halves, only one half of each sample type is shown. The microstructure of the sigma-containing sample shows little plastic deformation, appearing not very different from the microstructure of the as-received plate, except for some cracked individual particles and micro-crack formation within the  $\sigma$ -packets at larger particles (Figure 15c). The sigma-free sample exhibits gross plastic deformation, evident by the appearance of the grains which are elongated in the loading direction. Microvoids from the  $\sigma$ -free sample show the individual  $\sigma$ -particles that the voids formed around, as shown in Figure 15d. These microvoids occurred as a result of the presence of dispersed individual  $\sigma$ -particles as opposed to localized packets of  $\sigma$ -particles that caused large-scale premature fracture. From this observation, the resulting degradation of mechanical properties due to the presence of this sigma-phase is readily apparent. When the packets of  $\sigma$ -phase are not present, the austenite matrix grains are able to plastically deform, so much so that large microvoids are able to form at various locations within the sample. When packets of  $\sigma$ -phase are present, there are easy crack growth directions due to the presence of brittle (easily cracked)  $\sigma$ -particles located very near one another over microstructurally large distances across the sample, making the fracture process reach full rupture at comparatively lesser strain than if the packets were not present.



**Figure 15.** Cross-sections near the fracture surface of (a) a sigma-free tensile sample (LOM), (b) microvoids from a sigma-free sample (SEM), (c) a  $\sigma$ -containing tensile sample (LOM), and (d) a micro-crack formed due to a large particle from a  $\sigma$ -containing sample also showing cracked individual particles (SEM). Note that the loading direction (LD) is indicated.

The fracture surface of the sigma-containing sample (Figure 16a) exhibits plateaus, which are indicative of the crack leaving the plane of one sigma-phase packet for another, as in Figure 16b. Closer inspection of the surface of the plateaus reveals what appear to be cracked sigma particles (Figure 16c/d) correlating to the cracked particles seen in cross-section (Figure 15d). The fracture surface of a  $\sigma$ -free tensile sample (Figure 16e-g) displays microvoid coalescence, typical of a ductile fracture mechanism, which corroborates with the large amount of plastic deformation observed for this sample orientation. The size of the microvoids in the sigma-free sample appear to be bimodal, the larger voids containing large particles inside them whereas the



**Figure 16.** Scanning electron micrographs of the fracture surface appearance for (a) a sigma-containing tensile sample exhibiting several plateaus, (b) a sigma-free tensile sample exhibiting ductile fracture appearance, (c) closer view of a sigma-containing tensile sample fracture surface showing plateau morphology, and (d) closer view of a sigma-free tensile sample fracture surface showing microvoid morphology.

interiors of the smaller voids could not be resolved sufficiently to observe their origin (note, however, that submicron particles may exist throughout the material and could cause the smaller microvoids). The appearance of the fracture surfaces of the  $\sigma$ -free and  $\sigma$ -containing samples merely corroborate what was discovered from the sample cross-sections, although the different view gives a necessary perspective on the different fracture processes for the two sample conditions.

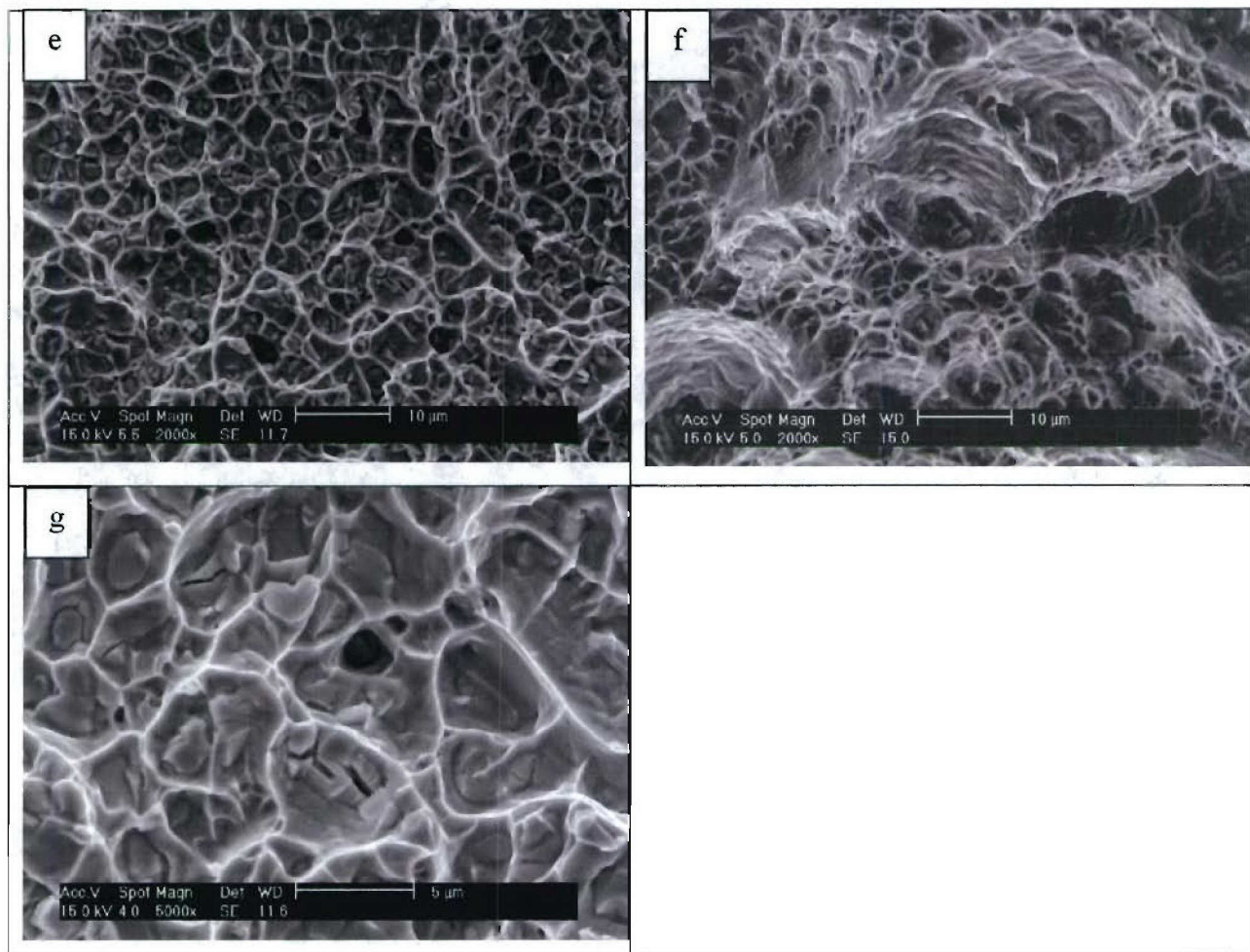


**Figure 16 continued:** Scanning electron micrographs of the fracture surface appearance for: (e) the plateau face appearance exhibiting cracked sigma particles on the sigma-containing tensile sample fracture surface, (f) the appearance of microvoid coalescence on the sigma-free tensile sample fracture surface showing a few particles within respective voids, and (g) a higher magnification image of a sigma-containing tensile sample fracture surface showing cracked sigma particles within each void.

Recently, the tensile properties of AL-6XN (containing  $\sigma$ -phase in microstructural bands) in various orientations were studied and it was found that the ductility in the short-transverse orientation was much lower than that for the long-transverse direction<sup>14</sup>. The decrease in ductility associated with the presence of the  $\sigma$ -phase was shown to originate with premature cracking of the  $\sigma$ -phase particles and preferential crack growth on planes of high particle content (associated with microstructural bands). The current work adds to this by showing that the reduced ductility is largely due to the presence of packets containing  $\sigma$ -phase and not solely due

to the short-transverse orientation, since the tensile properties were shown to decrease when the  $\sigma$ -phase packets were present in the samples over the  $\sigma$ -free condition.

### 2.2.2 Fracture Toughness Testing

Figure 17 shows the J-R curve representation of the J-integral fracture toughness data for the S-T( $\sigma$ ), S-T( $\sigma$ -free), L-T, and T-L sample orientations. It is important to recognize that these results are qualitative in nature since the sample sizes limited the region of valid data (dashed rectangle), in accordance with ASTM-E-1820, to values below which the differences in the fracture response of the samples are apparent. According to the standard, the maximum J-integral capacity for a specimen is given by the smaller of the following:  $J_{max}=b\sigma_Y/20$  or  $J_{max}=B\sigma_Y/20$ , where  $\sigma_Y=(\sigma_{YS} + \sigma_{TS})/2$ , b is the remaining un-cracked ligament of the sample (width W – crack length a), and B is the specimen thickness. This “limit” to the valid data is somewhat conservative considering that the requirements for plane-strain conditions for J testing occurs when  $J \leq B\sigma_{YS}$  (Broek 1978). Additionally, the maximum crack extension capacity for a specimen is given by the following:  $\Delta a_{max}=0.25b_0$ , where  $b_0$  is the original remaining ligament (width W – original crack length). In order to determine valid  $J_{IC}$  values, the 0.2-mm off-set construction line (parallel to and off-set from the blunting line) must intersect the J- $\Delta a$  curve within the region of valid data described above. This indicates that for the data shown in Figure 17, valid  $J_{IC}$  values could have been determined had the samples been large enough to move the dashed lines to values larger than the data experienced during the test. The difference in the curves for the S-T samples, however, does indicate that the through-thickness fracture properties are degraded by the presence of  $\sigma$ -phase particles in packet morphology.

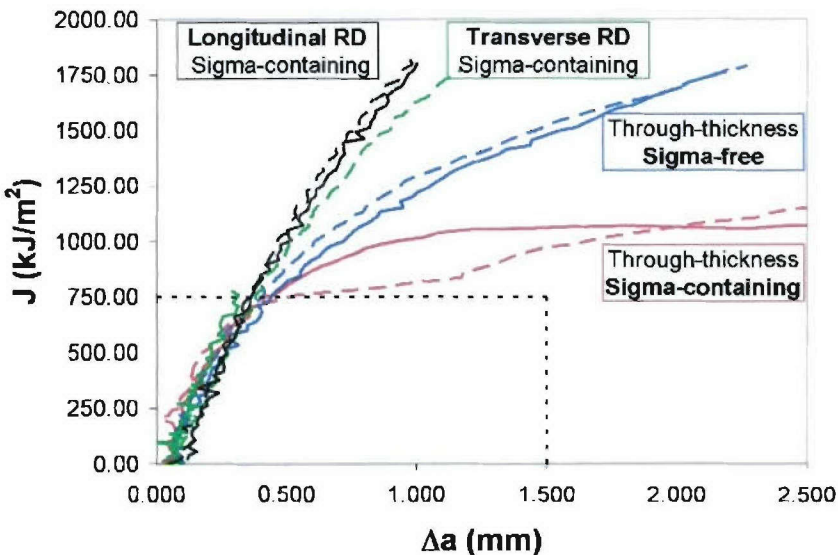


**Figure 17. J-R curve fracture toughness data for the S-T (sigma-containing and sigma-free), L-T, and T-L sample orientations**

Post-test characterization showed that the crack produced during the test grew along  $\sigma$ -phase packets in the  $\sigma$ -containing samples. When viewed in cross-section, the crack was observed to appear in a stepped pattern, since the packets occurred both in a discontinuous fashion and at various positions relative to the centerline of the plate, see Figure 18a. Notice that the crack travels from one packet to another either because (1) the previous packet it was traveling along ended or (2) a micro-crack had likely already formed within a packet on a different plane which linked to the macro-crack. Additionally, it was observed that many of the  $\sigma$ -phase particles had cracked one or more times, independently of the matrix material (Figure 18c). An energy dispersive spectrum (EDS) taken of an area from one of the packets shows higher levels of Cr and Mo than present in the matrix material, indicative of sigma or chi -phases (Figure 18e-f). However, it has been shown<sup>14</sup> that sigma-phase predominates over chi-phase in this alloy. The observation of cracked  $\sigma$ -particles is not surprising considering that  $\sigma$ -sigma is an intermetallic phase, which tends to be brittle in nature and not capable of sustaining much plastic deformation prior to fracture.

An alternative view from the fracture surface (Figure 19a-b) exhibits similar plateaus to that seen for the tensile specimens, which are indicative of the crack leaving the plane of one  $\sigma$ -phase packet for another. Figure 20a shows a higher magnification image that is representative

of the appearance of the face of the steps on the fracture surface of the  $\sigma$ -containing samples. Portions of the cracked particles that make up the packets remain on the surface. This is expected since the presence of multiple cracking of particles, as seen earlier in Figure 18c, indicates that the particle/matrix interface cohesion is strong<sup>21</sup> and are therefore not likely to fall out as is typically the case for microvoid formation where the particles de-cohere from the matrix. In contrast, the sigma-free samples exhibited a ductile tearing fracture mechanism in cross-section (Figure 18b) and the fracture surface corroborates this with what appear to be microvoids instead of flat plateaus (Figure 19c-d and Figure 20b). Figure 20c-d represent EDS data taken from a cracked  $\sigma$ -particle and the matrix material, respectively, from the fracture surface of a S-T( $\sigma$ ) sample.

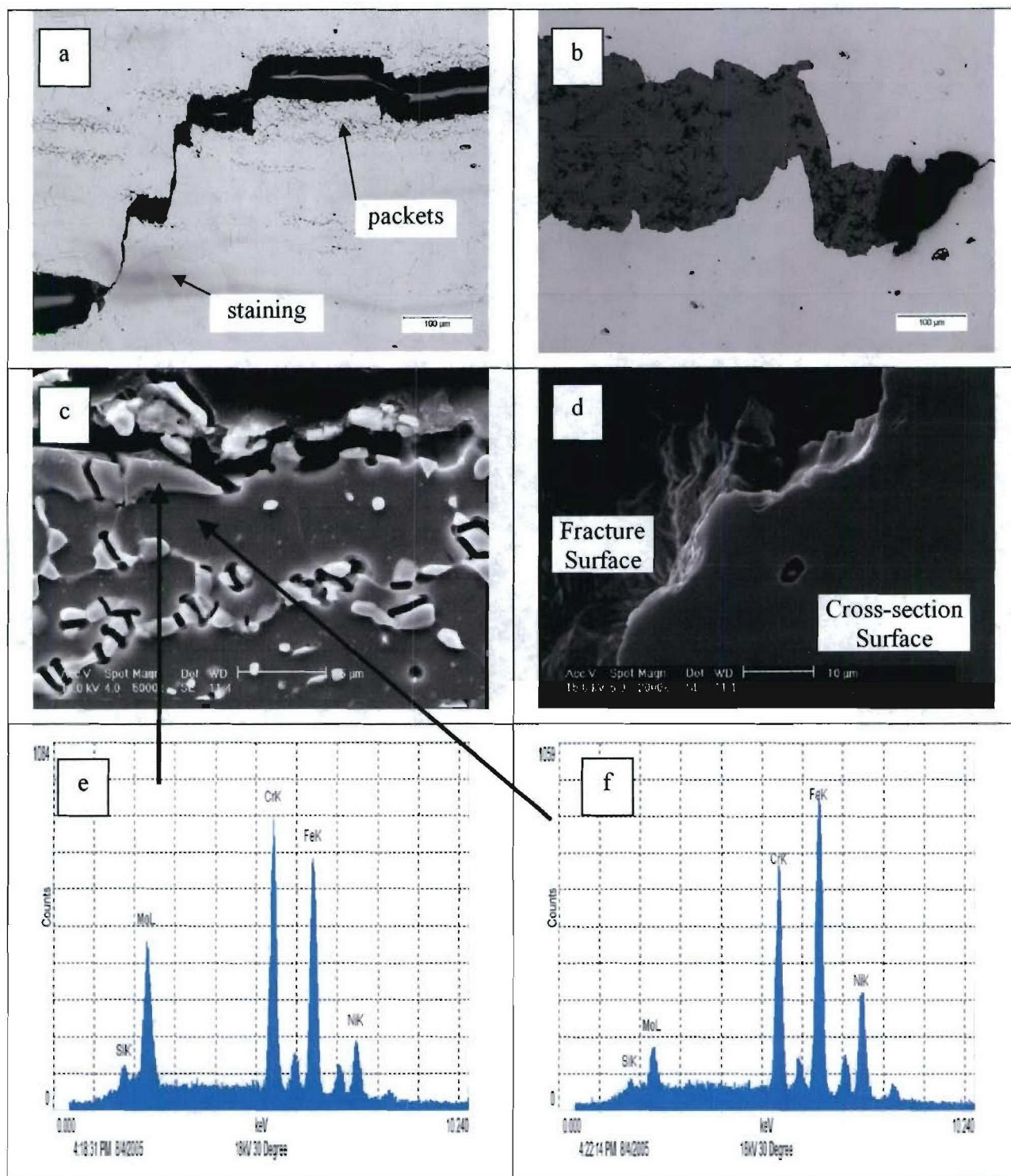


**Figure 18.** Microstructural cross-sections of the (a) sigma-containing and (b) sigma-free fracture toughness samples post-test (LOM). Scanning electron microscope images of (c) the cross-section of a sigma-containing fracture toughness sample showing cracked particles and (d) the cross-section of a sigma-free fracture toughness sample showing ductile tearing appearance. Energy Dispersive Spectra for (e) a particle and (f) the austenite matrix.

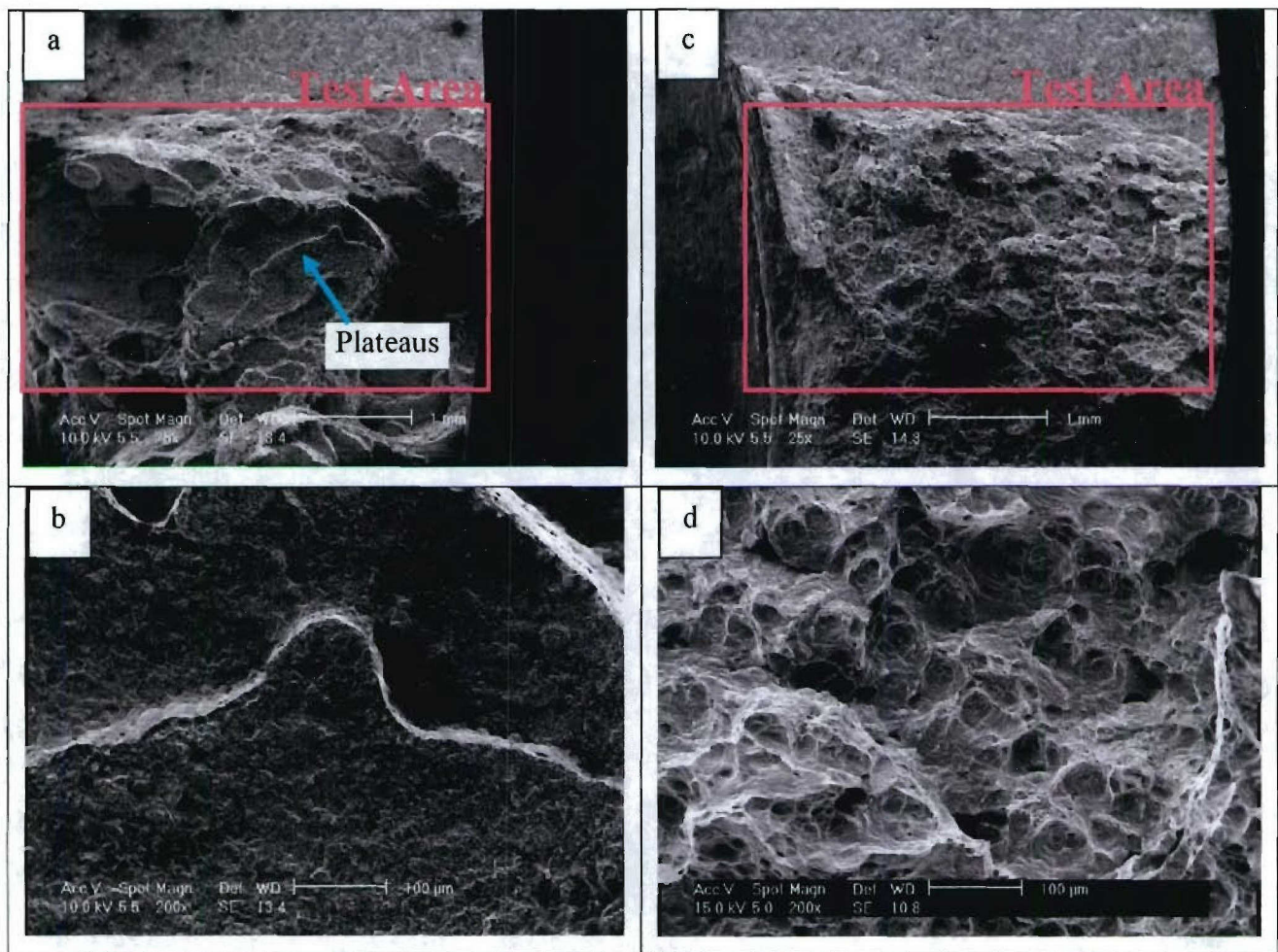


**Figure 19.** Low Magnification fracture surface appearance of fracture toughness samples for the two S-T orientations as viewed in the SEM: (a) sigma-containing and (b) sigma-free. The red rectangle indicates the fracture surface created during the test. Fracture surface appearance of fracture toughness samples for the two through-thickness orientations as viewed in the SEM: (c) sigma-containing showing plateau morphology and (d) sigma-free showing microvoid coalescence.

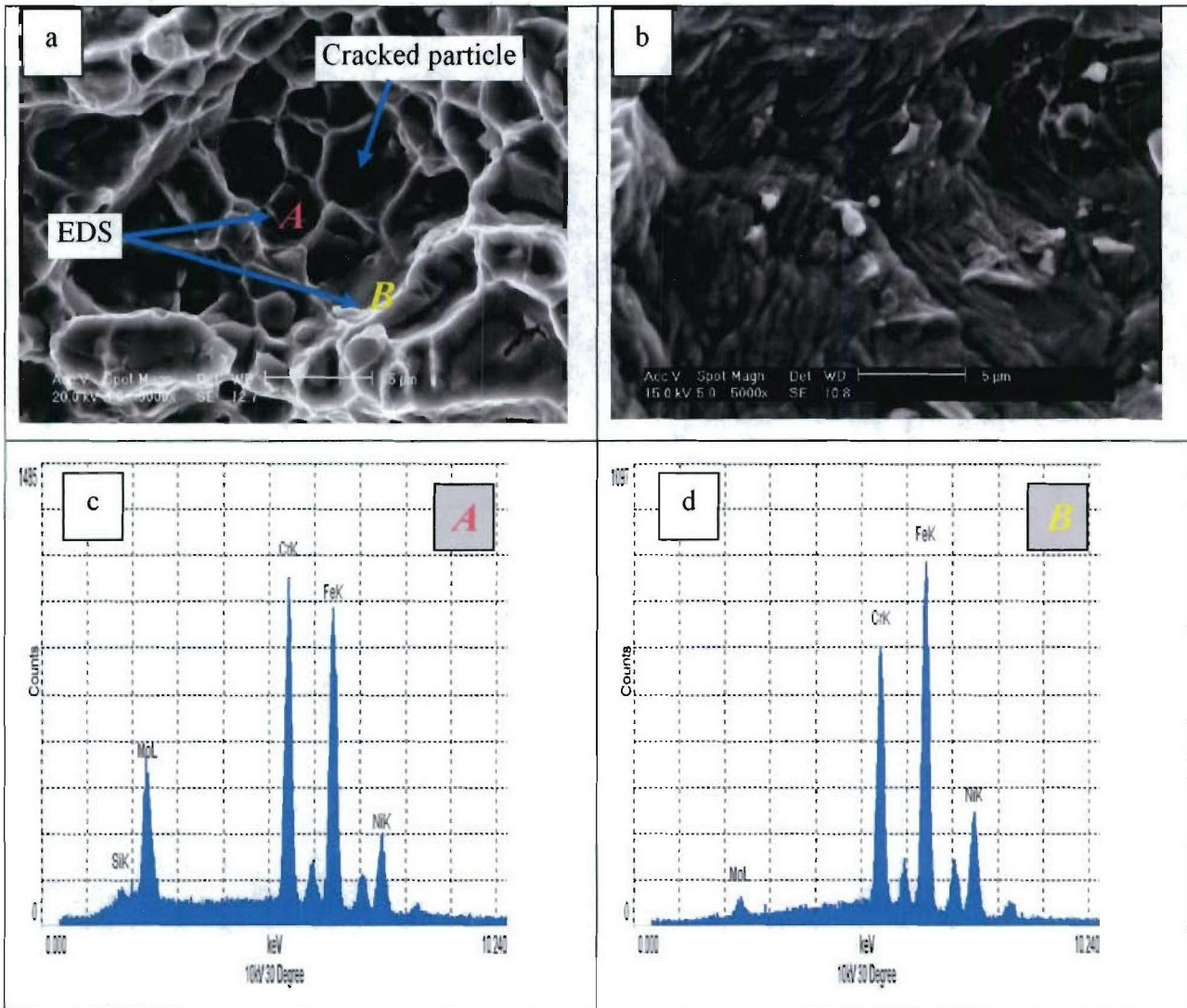


**Figure 20.** Fracture surface appearance of fracture toughness samples for the two through-thickness orientations as viewed in the SEM: (a) this sigma-containing sample shows cracked particles, (b) this sigma-free sample shows small particles within large microvoids, (c) EDS data from particle labeled ‘A’ in figure (a), and (d) EDS data from matrix region labeled ‘B’ in figure (a).

In comparison, the fracture response in the longitudinal and transverse rolling directions (RD) remains greater than both through-thickness conditions even though sigma phase is present in all samples except for the through-thickness S-T( $\sigma$ -free) condition. The portion of the crack front that encounters the sigma phase in the longitudinal and transverse orientations is very small compared to the through-thickness sigma-containing samples. This is because the longitudinal and transverse specimens were obtained from the 15.9-mm-thick plate of AL-6XN, for ease of fabrication; however, the sigma-phase was present closer to the centerline of the plate and not spread over as wide of a range surrounding the centerline as is the case for the 25.4-mm-thick

plate. Coupling what was previously mentioned with the fact that fracture toughness is greatly affected by crystallographic and microstructural anisotropy in plate materials and is generally greater in the longitudinal (T-L) and transverse (L-T) directions compared to the through-thickness (S-T) orientation depending on the rolling schedule, the result is not very surprising (Hertzberg p.416 and W.G. Ferguson, 1980). No microstructural evidence was found for the L-T and T-L sample orientations, so crystallographic anisotropy is likely the controlling factor.

### 2.2.3 *Apparent Fracture Process*

The fracture process in the short-transverse sample orientation, determined from the behavior of the tensile and fracture toughness samples, can be summarized as follows: (1)  $\sigma$ -phase particles crack under little tensile strain, presumably at larger particles first, followed by smaller ones, (2) if  $\sigma$ -phase packets are not present, as in the  $\sigma$ -free samples, the matrix austenite grains will plastically deform, creating micro-voids around whatever particles are present, leading to a microvoid coalescence fracture mechanism, (3) if  $\sigma$ -phase packets are present, as in the  $\sigma$ -containing samples, the adjacent  $\sigma$ -phase particles that are cracked leave little surrounding matrix material between them to support further stress, leading to rapid microvoid coalescence along the plane of a  $\sigma$ -phase packet (provided the crack that now separates each half of a cracked particle can be considered a microvoid), and (4) since the  $\sigma$ -phase packets do not occur on the same plane, the crack formed during fracture will change planes if the end of a packet is encountered to allow the crack to propagate in the same direction, but along a plane of easier crack extension.

### 2.2.4 *Fatigue Testing*

Figure 21 shows the closure-corrected fatigue data for the S-T( $\sigma$ ), S-T( $\sigma$ -free), (L-T), (T-L) sample orientations. The data show that the fatigue crack propagation (FCP) behavior of the L-T and T-L orientations is nearly identical to that for the S-T( $\sigma$ ) orientation. Additionally, the S-T( $\sigma$ -free) orientation displays a slight improvement in the FCP behavior, especially just above threshold, than for the other orientations which all contained  $\sigma$ -phase packets. Note that

microstructural effects are also typically apparent at very large growth rates and  $\Delta K$  values, but were never attained in the current research due to equipment limitations.

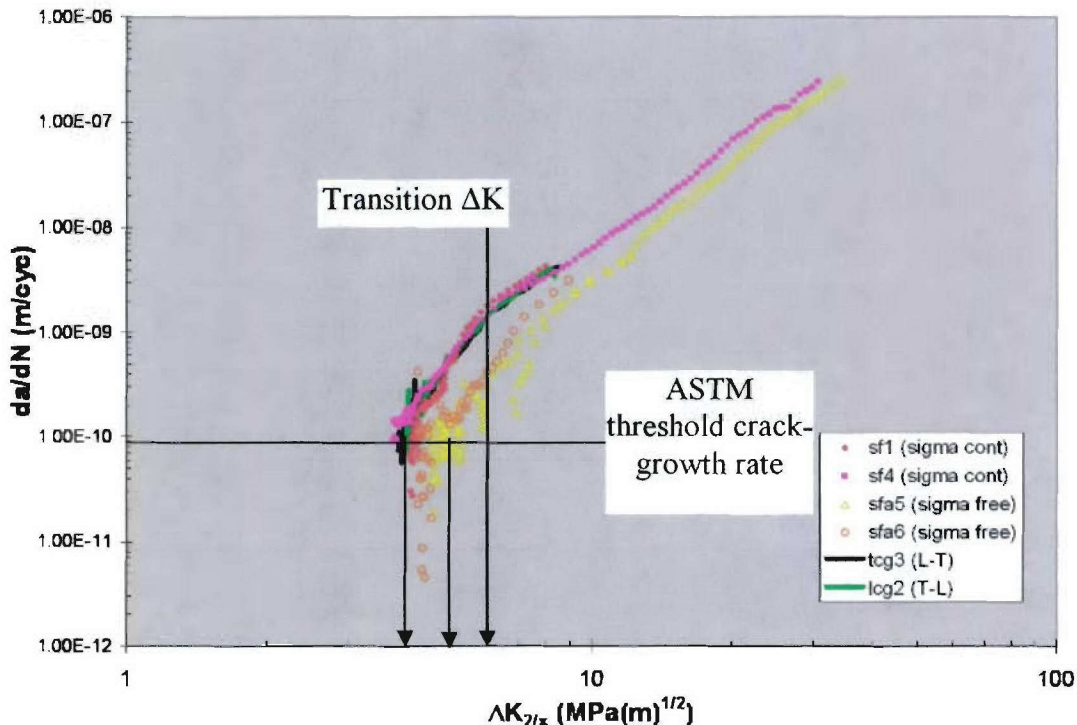


**Figure 21. Closure-corrected fatigue data for the sigma-containing (S-T), sigma-free (S-T), transverse RD (L-T), longitudinal RD (T-L) sample orientations using Paris'  $2/\pi$  correction procedure. The ASTM E-647 specified crack-growth rate is depicted, along with the apparent threshold  $\Delta K$  for the  $\sigma$ -containing / L-T / T-L and  $\sigma$ -free samples.**

The transition  $\Delta K$  value ( $\Delta K_T$ ), where the FCP behavior changes from structure insensitive that which is affected by the microstructure of the material, occurs when the cyclic plastic zone size ( $r_{cyc}$ ) ahead of the crack tip decreases to and below the controlling structural feature of the material. This is typically seen as a change in slope of the curve in the log-log plot as the fatigue curves near threshold values. The  $\Delta K_T$  for the above data appears to occur at approximately  $6 \text{ MPa}(\text{m})^{1/2}$ , which correlates to a  $r_{cyc}$  of  $8.23 \mu\text{m}$  for this alloy, using equation (4). The measured grain size for the two S-T orientations was approximately  $32 - 42 \mu\text{m}$ , obtained manually using ASTM-E-562<sup>22</sup> Abrams' method. This measured grain size range would be expected to show its transition around  $11.8 - 13.6 \text{ MPa}(\text{m})^{1/2}$ . Note that twins were disregarded as best as possible in the grain size calculation, although twins are rather prevalent in

the microstructure of this alloy and could conceivably reduce the  $\Delta K_T$  value, since the  $r_{cyc}$  would need to be smaller, and correlate to the  $\Delta K_T$  observed in the data.

As seen in Figure 21, the threshold  $\Delta K$  was approximately  $4 \text{ MPa(m)}^{1/2}$  for the L-T, T-L, and S-T( $\sigma$ ) orientations and approximately  $5 \text{ MPa(m)}^{1/2}$  for the S-T( $\sigma$ -free) orientation, as defined by ASTM-E-647 to occur at  $10^{-10} \text{ m/cyc}$  crack growth rate (which nears atomic scale dimensions). This is significant considering that the  $r_{cyc}$  that correlates to these threshold values are 3.7 and 5.7  $\mu\text{m}$  (by equation (4)) for the S-T( $\sigma$ ) and S-T( $\sigma$ -free) orientations, respectively. These values lie roughly equivalent to the typical sigma-phase particle size observed for these alloys<sup>14</sup> reported the sigma particle size to be  $\leq 10 \mu\text{m}$ . However, the appearance of the  $\sigma$ -phase particles in Figure 10b and 18c seem to be mostly smaller than the threshold  $r_{cyc}$  value for the particular heat of AL-6XN used in this study.

Note that the Paris 2/pi correction procedure was applied to the raw fatigue data to account for damage that is accumulated when the crack is partially closed. The traditional  $\Delta K_{eff}$  using the opening load ( $\Delta K_{eff} = K_{max} - K_{op}$ ) was shown to overestimate the actual fatigue crack propagation behavior since it assumed that cracked could only propagate when the crack is fully open. The 2/pi correction was chosen due to its simplicity and availability of data to employ it; other correction procedures could not be used due to equipment limitations.

Figure 22 shows a cross-section of the end of the fatigue curves, which correlate to the threshold regime for  $\sigma$ -containing and  $\sigma$ -free samples, respectively. They are virtually indistinguishable, especially since very little  $\sigma$ -phase is observed for the “ $\sigma$ -containing sample.” For this particular sample cross-section, the largest density of  $\sigma$ -packets does not occur on the same plane as the C(T) specimen starter notch or fatigue crack. This could possibly be due to inaccurate preparation of the sample, or that the cross-section shown does not contain very much sigma-phase near the fatigue crack. In either case, the modest improvement in the FCG response for  $\sigma$ -free samples may simply be due to the slightly larger grain size observed in the region of the sample that the fatigue crack traversed compared to the grain size of the  $\sigma$ -containing sample (42 vs. 32  $\mu\text{m}$  using ASTM E-562) as seen cross-section from the center thickness of the sample. Larger grain sizes cause higher threshold  $\Delta K$  values since the critical plastic zone size for microstructural influence would be reached at higher  $\Delta K$  values due to roughness-induced crack closure. In addition, since the  $\sigma$ -phase particles are much smaller than the austenite grain size,

no effect might be expected. Given that the  $\Delta K$  values corresponding to such a small plastic zone size, as that required for  $\sigma$ -phase particle influence, are not expected to be attained because the threshold region has been shown to be a function of the much larger austenite grain size for this material. This austenite grain size dependence of threshold in AL-6XN was also shown by Kusko<sup>18</sup>. Additionally, no evidence of sigma-phase influence could be observed from the fracture surface appearance of the  $\sigma$ -containing samples, as shown in Figure 22.

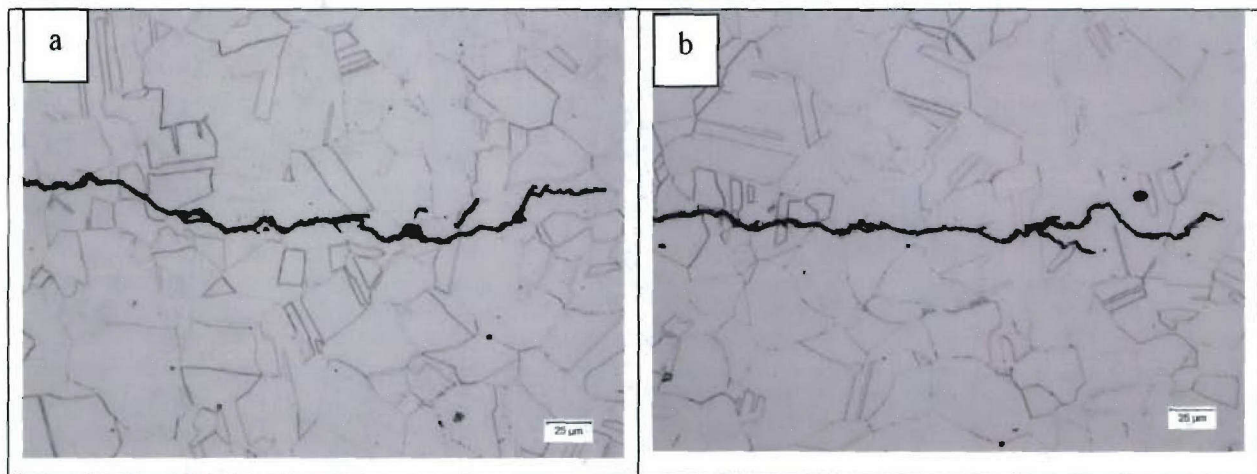


**Figure 22. Fatigue cracks for the through-thickness (a) sigma-containing and (b) sigma-free samples at threshold (LOM).**

## Reference List

1. J.Sikora and E.Devine. Construction Cost Study of an Advanced Double Hull DDG-51, NSWCCD Report TR-65-97/32. 1997.
2. S. Banovic, J. DuPont, and A. Marder, Dilution Control in Gas Tungsten Arc Welds Involving Superaustentic Stainless Steels and Nickel Based Alloys. *Metallurgical and Material Transactions* **32B**, 1171-1176 (2001).
3. S. Banovic, J. DuPont, and A. Marder, Dilution and microsegregation in dissimilar metal welds between super austenitic stainless steel and nickel base alloys. *Science and Technology of Welding and Joining (UK)* **7**, 374-383 (2002).
4. S. Banovic, J. DuPont, and A. Marder, Microstructural Evolution and Weldability of Dissimilar Welds between a Super Austenitic Stainless Steel and Nickel-Based Alloys. *Welding Journal* **82**, 125-135 (2003).
5. J. DuPont, L. Friedersdorf, A. Marder, and S. Banovic. Weldability and Corrosion Performance of Welds in AL-6XN Superaustenitic Stainless Steel. Lehigh University ATLSS Report No. 01-03. 2001.
6. J. Brooks and A. Thompson, Microstructural Development and Solidification Cracking Susceptibility of Austenitic Stainless Steel Welds. *International Materials Reviews* **36**, 16-44 (1991).
7. J. Elmer, S. Allen, and T. Eagar, Microstructural Development During Solidification of Stainless Steel Alloys. *Metallurgical Transactions A* **20A**, 2117-2131 (1989).
8. B. Sundman. Thermo-Calc. S-100 44[[N]]. 2001. Stockholm, Sweden, Department of Materials Science and Engineering, KTH.
9. N. Saunders. Fe-Data Thermodynamic Database. [[3.0]]. 2001. The Surrey Research Park, Guildford, UK, Therrnotech, Ltd.
10. A. Schaeffler, Constitution Diagram for Stainless Steel Weld Metal. *Metals Progress* **56**, 680-680B (1949).
11. S. Katayama and A. Matsunawa. Proceedings of ICALEO. 60-67. 1984.
12. M. Perricone, A. Marder, A. Benscoter, J. Regina, and J. DuPont. *Failure Analysis of Fillet Welded AL-6XN Box Beam for ATLSS*. 2005. Lehigh University, Dept. of Materials Science and Engineering: Bethlehem, PA 18015.
13. E-8-04, A., *Standard Test Methods for Tension Testing of Metallic Materials*, ASTM: West Conshohocken, PA. 2005.
14. A. Stauffer, D. Koss, and J. McKirgan, *Microstructural Banding and Failure of a Stainless Steel*. *Metallurgical and Materials Transactions A* **35A**, 1317-1324 (2004).
15. E-1820-05, A., *Test Method for Measurement of Fracture Toughness*: ASTM: West Conshohocken, PA. 2005.
16. E-399, A., *Standard Test Method for Linear-Elastic Plane-Strain Fracture Toughness KIC of Metallic Materials*: ASTM: West Conshohocken, PA. 2005.
17. E-647, A., *Standard Test Method for Measurement of Fatigue Crack Growth Rates*: ASTM: West Conshohocken, PA. 2005.

18. C. Kusko, J. DuPont, and A. Marder, *Influence of Stress Ratio on Fatigue Crack Propagation Behavior of Stainless Steel Welds*. *Welding Journal* 59-64 (2004).
19. P. Paris, H. Tada, and J. Donald, *Service Load Fatigue Damage - A Historical Perspective*. *International Journal of Fatigue* 21, 35-46 (1999).
20. J. Donald, *Introducing the Compliance Ratio Concept for Determining Effective Stress Intensity*. *International Journal of Fatigue* 19 (Supplement 1), 191-195 (1997).
21. Q. Wang, *Metallurgical and Materials Transactions A* 34A, 2887-2899 (2003).
22. E-562, A., *Standard Test Method for Determining Volume Fraction by Systematic Manual Point Count*. ASTM: West Conshohocken, PA. 2005.

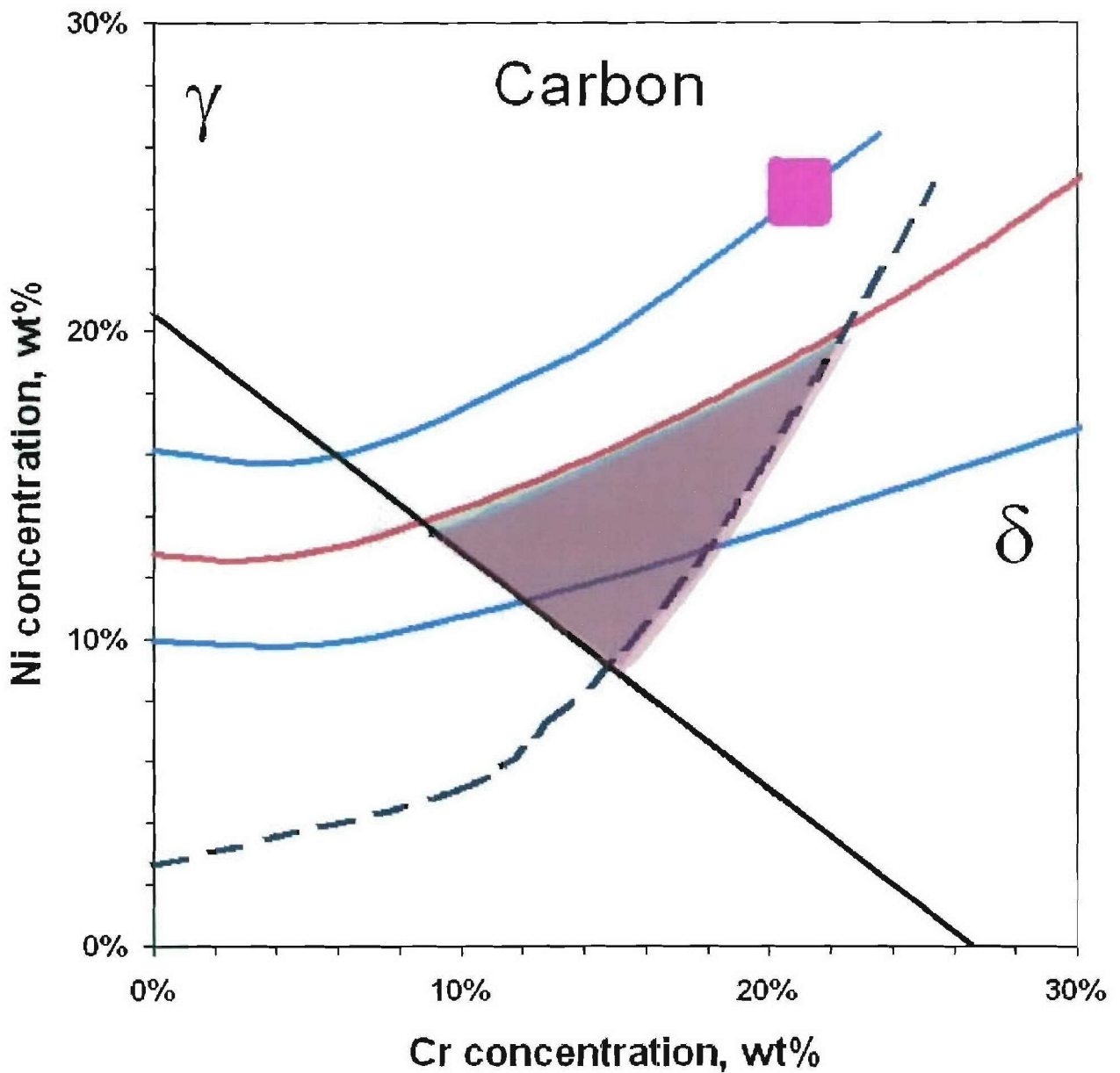


Figure 23. Phase stability diagram of Fe-Ni-Cr-6Mo compositions. Superimposed is the location and shape of the FA zone with 0.01wt% C (blue) and 0.02wt% C (red).

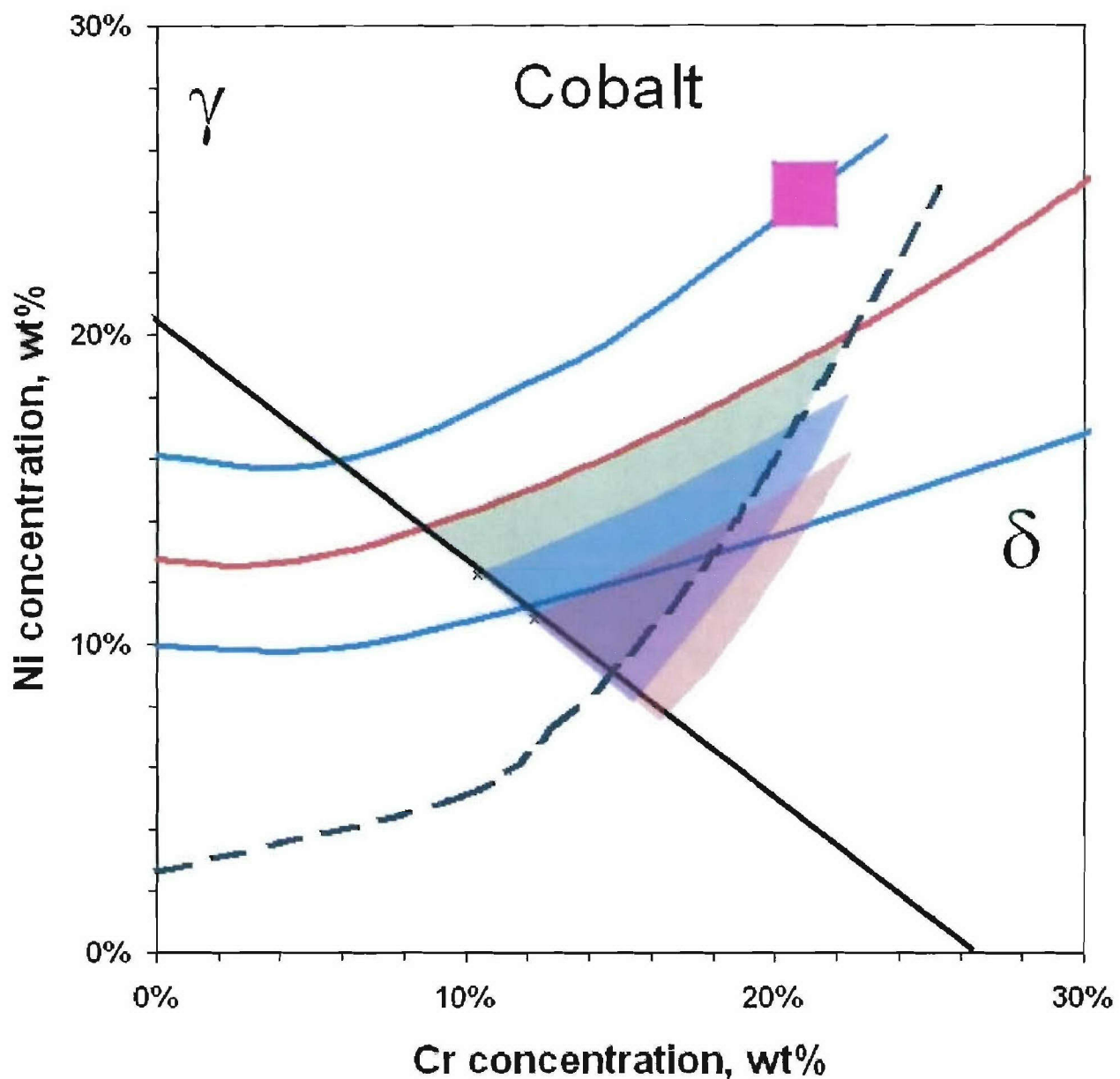
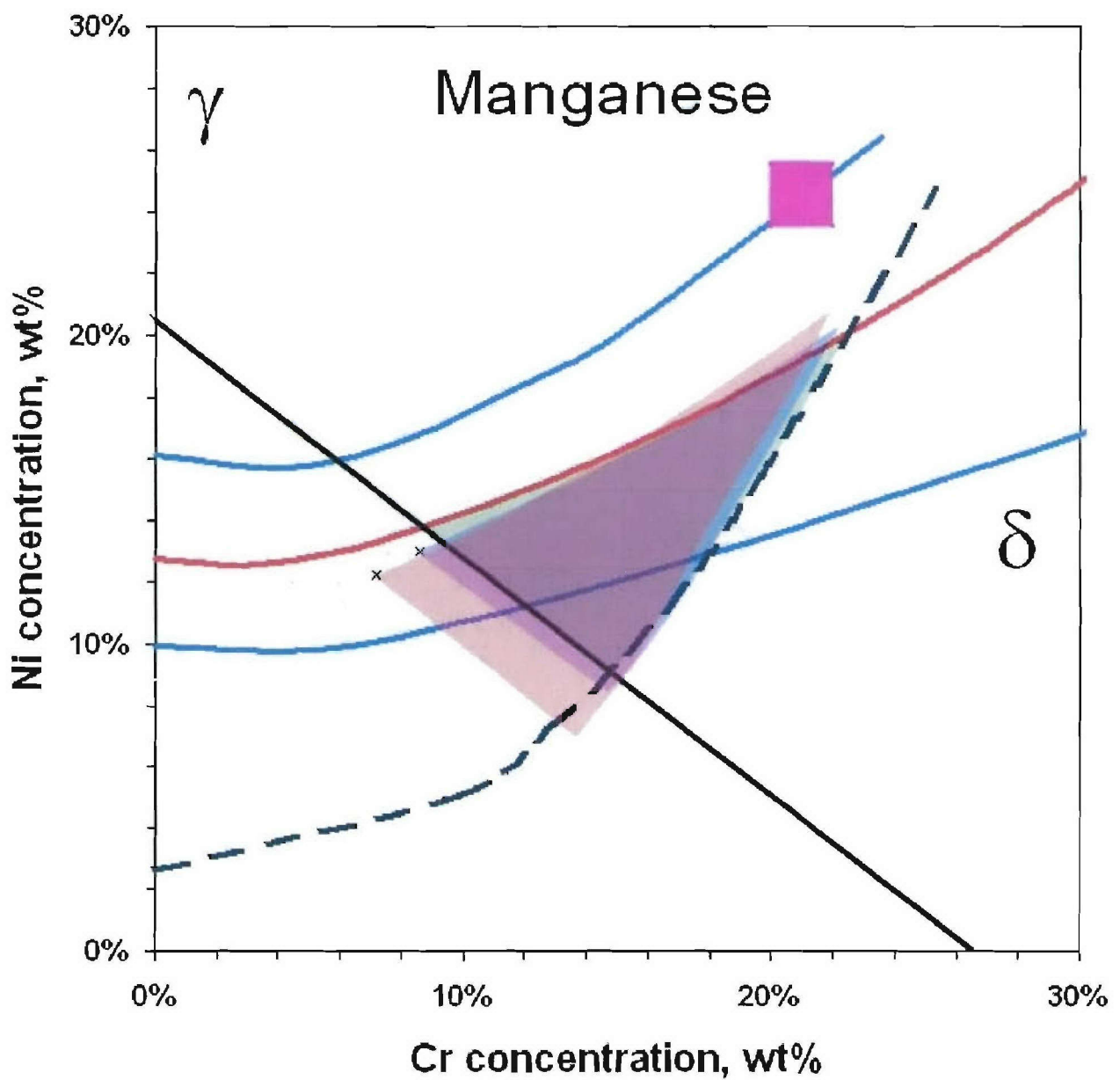


Figure 24. Phase stability diagram of Fe-Ni-Cr-6Mo compositions. Superimposed is the location and shape of the FA zone with 2wt% Co (blue) and 4wt% Co (red).



**Figure 25.** Phase stability diagram of Fe-Ni-Cr-6Mo compositions. Superimposed is the location and shape of the FA zone with 2wt% Mn (blue) and 4wt% Mn (red).

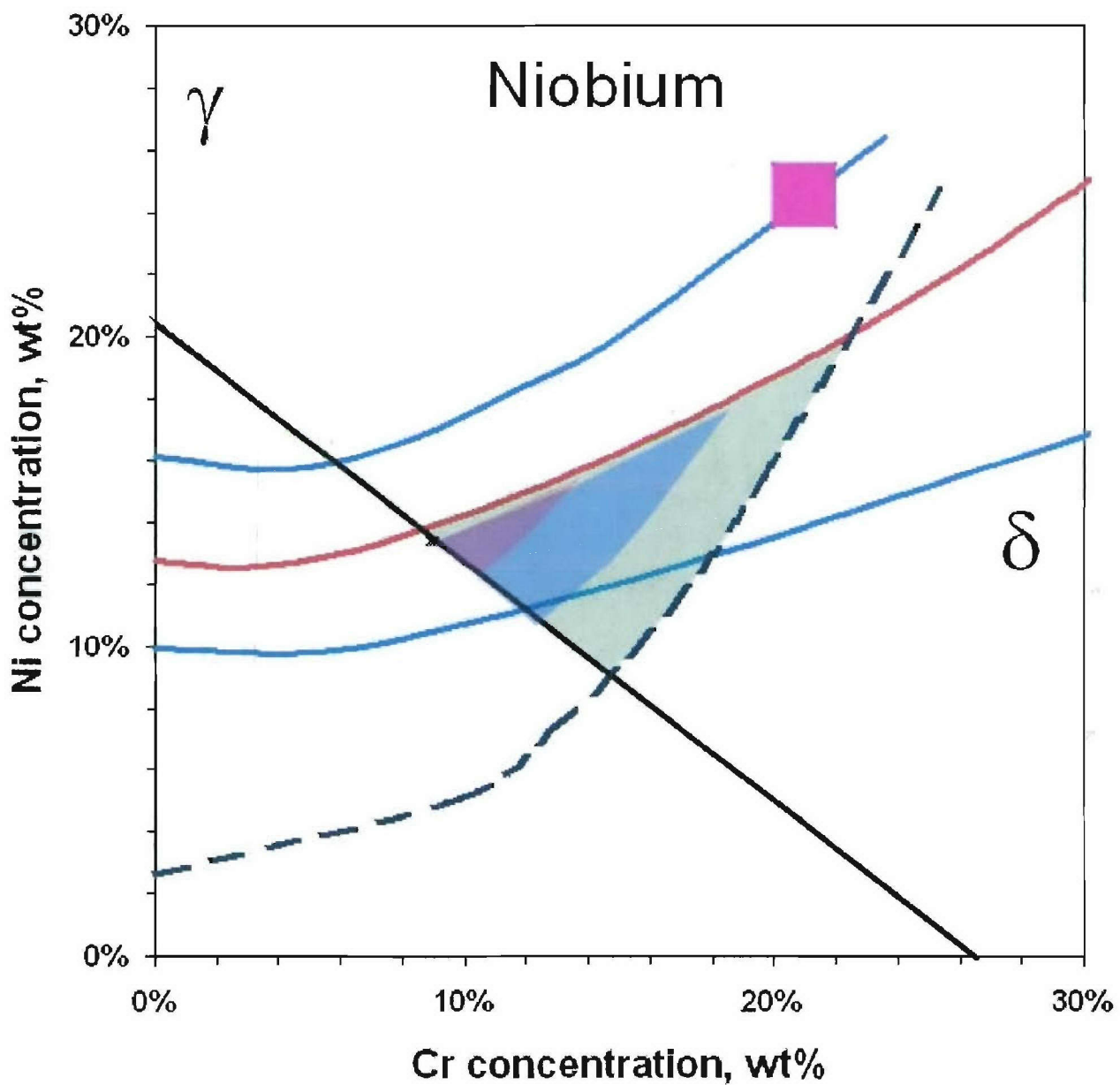


Figure 26. Phase stability diagram of Fe-Ni-Cr-6Mo compositions. Superimposed is the location and shape of the FA zone with 2wt% Nb (blue) and 4wt% Nb (red).

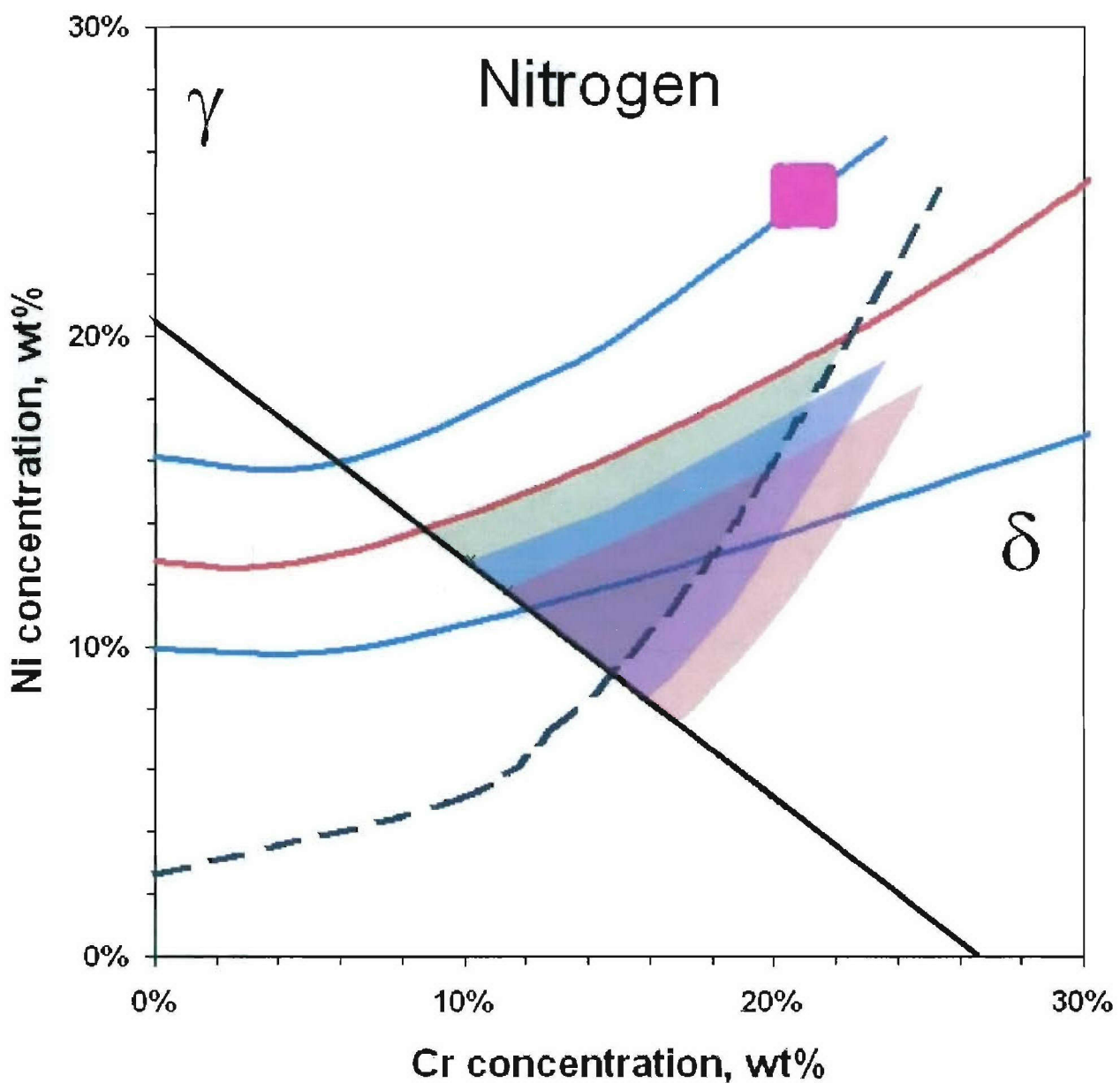
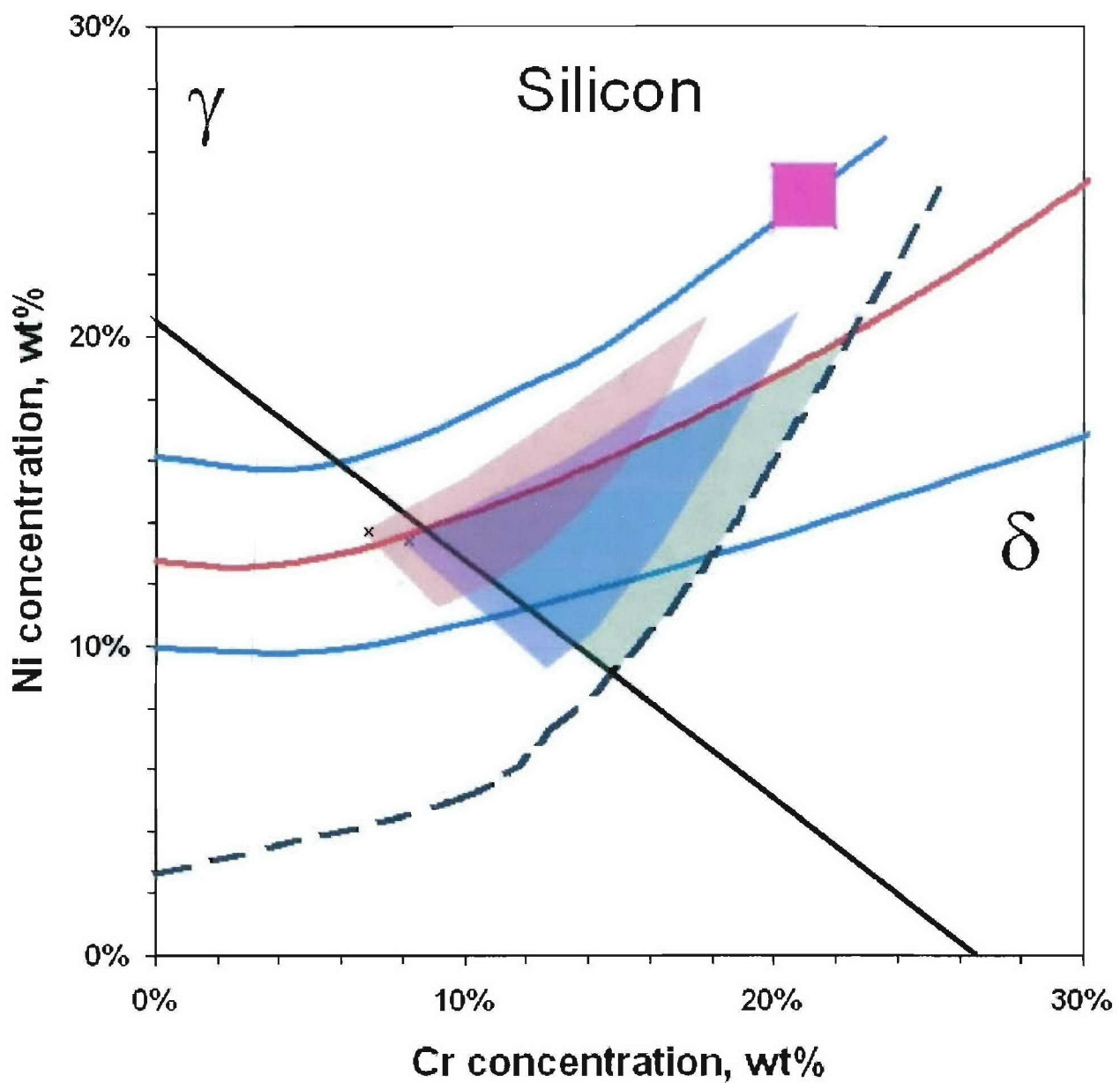
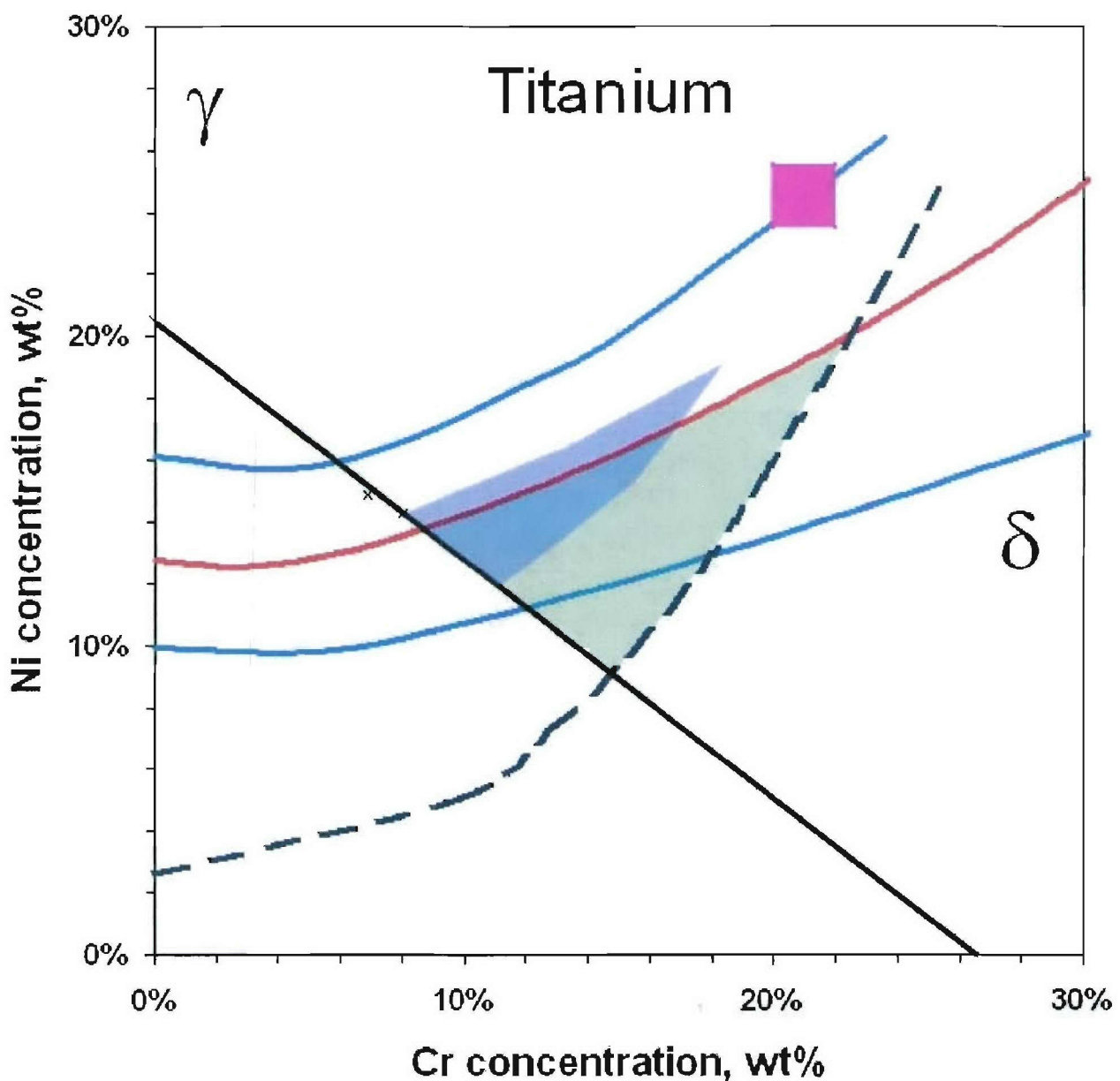


Figure 27. Phase stability diagram of Fe-Ni-Cr-6Mo compositions. Superimposed is the location and shape of the FA zone with 0.1wt% N (blue) and 0.2wt% N (red).



**Figure 28.** Phase stability diagram of Fe-Ni-Cr-6Mo compositions. Superimposed is the location and shape of the FA zone with 2wt% Si (blue) and 4wt% Si (red).



**Figure 29.** Phase stability diagram of Fe-Ni-Cr-6Mo compositions. Superimposed is the location and shape of the FA zone with 2wt% Ti (blue) and 4wt% Ti (red).

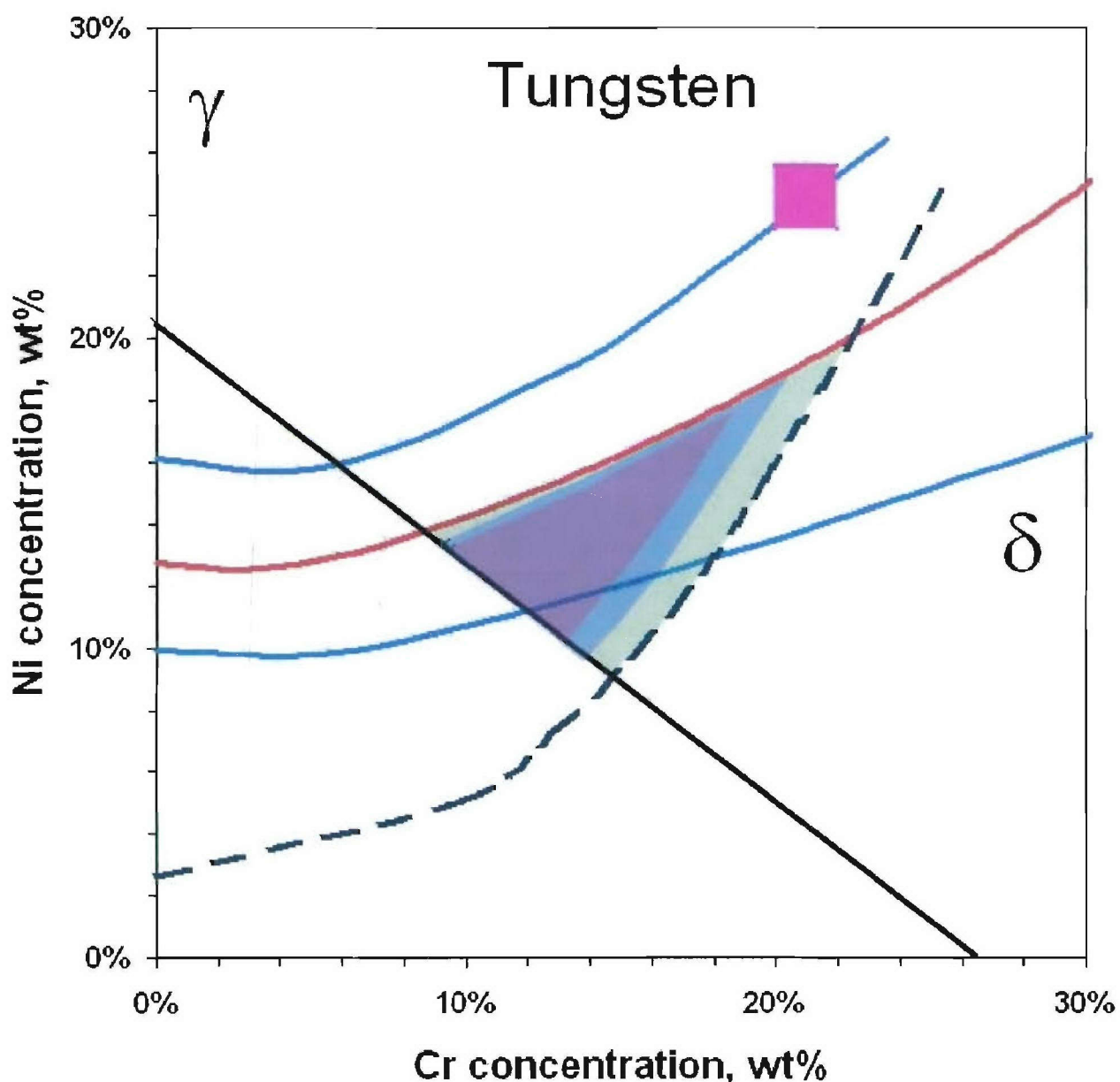


**Figure 30.** Phase stability diagram of Fe-Ni-Cr-6Mo compositions. Superimposed is the location and shape of the FA zone with 2wt% W (blue) and 4wt% W (red).

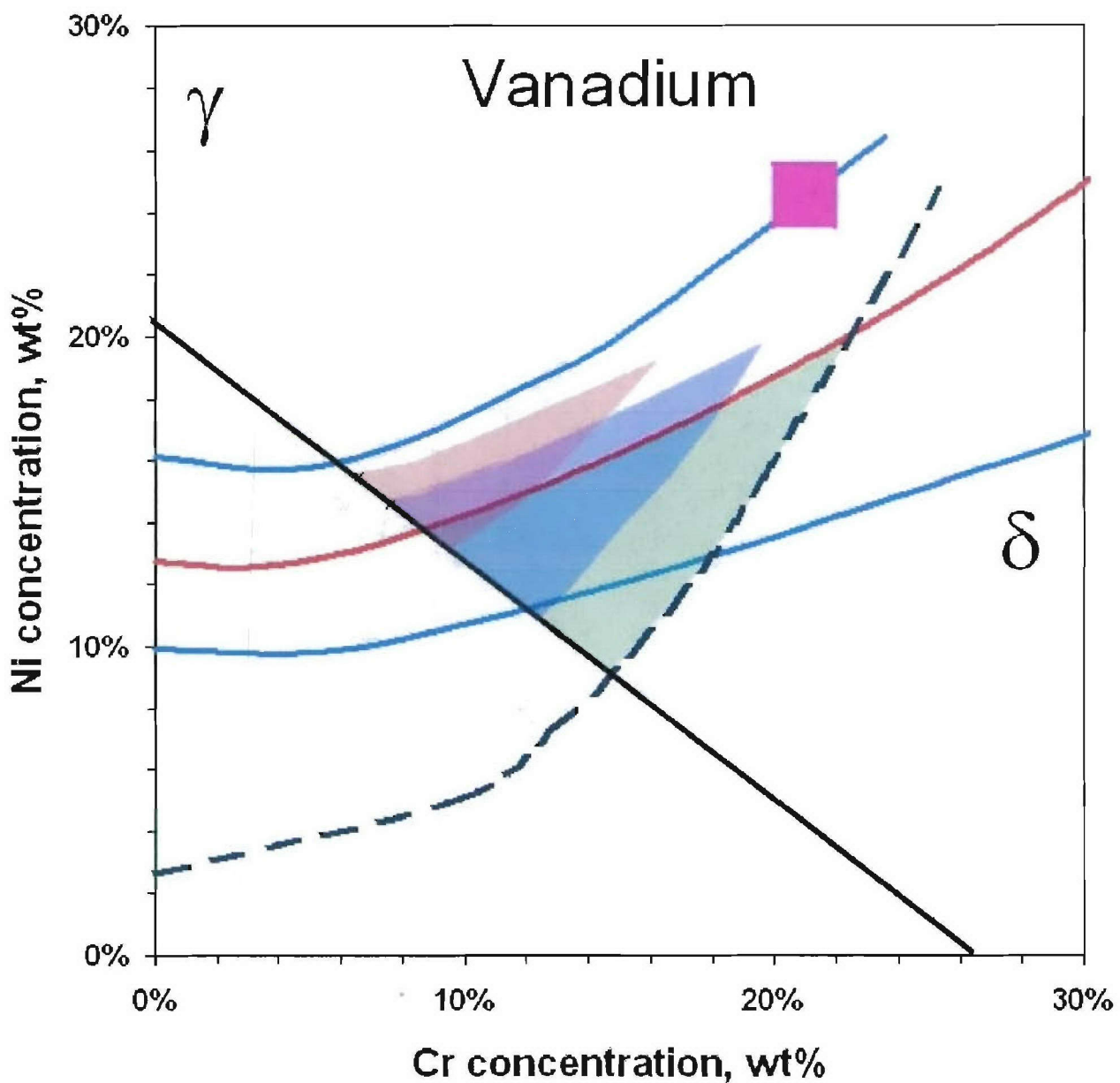


**Figure 31.** Phase stability diagram of Fe-Ni-Cr-6Mo compositions. Superimposed is the location and shape of the FA zone with 2wt% V (blue) and 4wt% V (red).

## PUBLICATIONS

1. M.J. Perricone, J.N. DuPont, and M.J. Cieslak. "Solidification of Hastelloy Alloys: an Alternative Interpretation", Metallurgical and Materials Transactions A, Vol. 34A, May 2003. p.1127.
2. M.J. Perricone, T.D. Anderson, and J.N. DuPont. "Effect of Composition on the Solidification Behavior of Several Ni-Cr-Mo and Fe-Ni-Cr-Mo alloys" accepted for publication in Metallurgical and Materials Transactions A.
3. T.D. Anderson, M.J. Perricone, and J.N. DuPont. "The Influence of Molybdenum on the Microstructure of Stainless Steel Welds." being prepared for Metallurgical and Materials Transactions A.
4. M.J. Perricone, J.N. DuPont. "The Influence of Composition and Cooling rate on the Massive Transformations in Stainless Steel Welds", being prepared for Metallurgical and Materials Transactions A.
5. T.D. Anderson, M.J. Perricone, and J.N. DuPont. "Development of Filler Metals for Super Austenitic Stainless Steels." Trends in Welding Research 2005, conference proceedings.

## THESES

M.J. Perricone. "Effect of Composition, Cooling Rate, and Solidification Velocity on the Microstructural Development of Mo-bearing Stainless Steels." Doctoral Dissertation. Lehigh University, 2005.

T.D. Anderson. "Microstructural Development of Mo-bearing Stainless Steel Alloys." Master's Thesis. Lehigh University, 2005.

K.D. Adams. "The Influence of Sigma Phase on the Fatigue and Fracture Behavior of Alloy AL6XN" Master's Thesis. Lehigh University, 2005.

## AWARDS

T.D. Anderson - American Welding Society – Navy Joining Center Graduate Research Fellowship. "Alloy Development of a Robust Filler Metal for the Superaustenitic Stainless Steel AL-6XN.

## Budget Summary

	<u>Budget</u>	<u>Actual</u>
Faculty Summer Salary	23,074	3,000
Technicians		6,570
Graduate Research Asst. Stipend	38,938	26,275
Graduate Research Asst. Tuition	19,600	4,805
Employee Benefits	<u>7,932</u>	<u>3,233</u>
<b>Total Salaries and Wages</b>	<b>\$89,544</b>	<b>\$43,883</b>
Travel	2,000	4,761
Materials and Supplies	2,500	11,296
Publications/Communications	2,500	431
Equipment Use	4,500	33,611
Testing and analysis	<u>8,000</u>	<u>9,612</u>
	\$19,500	\$59,711
<b>Total Direct Costs</b>	<b>\$109,044</b>	<b>\$103,594</b>
Indirect Costs (58.31%)	<u>52,155</u>	<u>57,605</u>
<b>TOTAL PROJECT COSTS</b>	<b>\$161,199</b>	<b>\$161,199</b>